

CALIBRATION OF A POLARIZED PROTON TARGET

by

RICKEY LEE SHYPIT

B.Sc., The University of Winnipeg, 1979

A THESIS SUBMITTED IN PARTIAL FULFILLMENT OF
THE REQUIREMENTS FOR THE DEGREE OF
MASTER OF SCIENCE

in

The Faculty of Graduate Studies
Department of Physics

We accept this thesis as conforming
to the required standard

The University of British Columbia
April, 1981

© Rickey Lee Shypit, 1981

In presenting this thesis in partial fulfilment of the requirements for an advanced degree at the University of British Columbia, I agree that the Library shall make it freely available for reference and study. I further agree that permission for extensive copying of this thesis for scholarly purposes may be granted by the head of my department or by his or her representatives. It is understood that copying or publication of this thesis for financial gain shall not be allowed without my written permission.

Department of Physics

The University of British Columbia
2075 Wesbrook Place
Vancouver, Canada
V6T 1W5

Date April 27/81

ABSTRACT

Proton polarization of a butanal 5% H_2O -EHBA- $\text{C}_r(\text{V})$ polarized target have been measured by elastic scattering to an accuracy of $\pm 2\%$. The four cubic centimeter target sample, suspended in a 25 KG field, was cooled by a pumped ^3He refrigerator. Left right asymmetry of scattered particles were detected by a two arm telescope, each arm consisting of a MWPC and a plastic scintillator. Separation of elastic two body events in hydrogen from non-elastic two body events in nonhydrogenous material was achieved using a coplanarity test.

TABLE OF CONTENTS

	<u>page</u>
I. INTRODUCTION	1
II. FORMALISM	6
2.1 The Scattering Matrix	6
2.2 Dynamic Nuclear Orientation	12
2.3 Q-meter Detection	17
III. APPARATUS	20
3.1 Polarimeter	20
3.2 Super Conducting Solenoid	23
3.3 Collimator	24
3.4 4B3 Bending Magnet	24
3.5 Quadrupole and Steering Magnets ..	26
3.6 Monitor 4CM8	27
3.7 Polarized Target ...	27
3.8 NMR System	30
IV. THE POLARIZATION MONITOR	32
V. DATA ACQUISITION	39
VI. DATA ANALYSIS	45
6.1 Reconstruction of Proton Tracks ..	45
6.2 Background Subtractions ...	51
6.3 The Fitting Equation	56
6.4 Error Analysis	60
VII. RESULTS AND CONCLUSION	63
7.1 Results	63
7.2 Conclusion ..	69

LIST OF TABLES

		<u>page</u>
3.1	Solenoid Currents Calculated to effect a 90° Precession	25
3.2	Currents in the Bending Magnet Calculated for a 35° Bend	25
5.1	Precise Beam Energies in MeV (at extrac- tion, at the polarimeter, after the polari- meter, and at the target	44
6.1	Run Averaged Hydrogen to Background Ratios	55
6.2	Precession Angle ψ in the Bending Magnet	55
6.3	Values of the Polarization Parameter at 26° LAB	59
7.1	Final Values of A , $\bar{\theta}$ and $\delta A(\bar{\theta})$	64
7.2	Final Values of \bar{C}	65
7.3	NMR Polarization Integrals and Absolute Target Polarizations	66

LIST OF FIGURES

		<u>page</u>
2.1	Kinematic Diagram	8
2.2	Energy Level Diagram	16
3.1	Beamline 4C	21
3.2	Beamline Polarimeter	22
3.3	NMR Functional Diagram	28
3.4	Schematic of the Cryostat	29
4.1	Polarization Monitor	33
4.2	Three Beam Defining Scintillators ...	35
4.3	Electronic Logic Diagram	36
4.4	Diagram of a Delay-Line Multi-Wire Proportional Chamber	37
5.1	Scope Trace Showing NMR Signal (Re- produced from Polaroid Photograph)	41
5.2	Attenuation In Beam Transmitted Through The Target	42
6.1	TDC Difference Histogram	47
6.2	Line Integral of the B Field	50
6.3	Coplanar Histogram	53

ACKNOWLEDGEMENT

I would like to thank my colleagues in this experiment who first introduced me to experimental nuclear physics - D. Axen, D.V. Bugg, M. Comyn, J. Edgington, D. Healey, G. Ludgate, J. Stanley, N. Stevenson, and N. Stewart. I also thank R. Dubois, P. Bennett and A. Haynes for their assistance with many computing problems.

I would especially like to thank my supervisor Dave Axen for his constant encouragement and advice during the experiment and throughout the writing of this thesis.

Chapter I

INTRODUCTION

The calibration of a polarized proton target by nuclear scattering techniques is described in this thesis. The calibration involved a measurement of the left right asymmetry in proton proton scattering with the beam and target aligned longitudinally. The measured asymmetry is given by a product of the beam polarization, the target polarization and the C_{LL} parameter. The C_{LL} parameter was computed from a phase shift analysis of the world data and the beam polarization was determined using a previously calibrated polarimeter. The target polarization extracted from this asymmetry measurement was then compared to the value of target polarization determined from an NMR measurement.

Measurements were made at beam energies of 210, 325, 425, 460, 500 and 520 MeV. The energy region covered by these measurements extends from the minimum to the maximum beam energy available at the TRIUMF cyclotron.

The measurement of target polarization by the nuclear scattering method was motivated by the need for an accurate determination of the target polarization which was required in the measurement of $\Delta\sigma_L$. $\Delta\sigma_L$ is the difference in proton proton total crosssections for spins aligned parallel and anti-parallel along the longitudinal direction. Previous measurements of $\Delta\sigma_L^{1,2,3,4}$ have relied only on nuclear magnetic resonance techniques to determine the target polarization. Inconsistencies in previously published data might be explained by systematic errors in the normalization of the target polarization. This experiment is essentially a test of that hypothesis.

In an NMR measurement the target polarization is determined from the following relation

$$P_T = \frac{\text{NMR enhanced signal}}{\text{NMR thermal signal}} \cdot P_{\text{thermal}}$$

where P_{thermal} is the absolute target polarization at thermal equilibrium. Thermal equilibrium refers to the state in which the nuclear spin system is in equilibrium with its surroundings. P_{thermal} is calculated from the fundamental Boltzman equation

$$P_{\text{thermal}} = \frac{\text{EXP}(\mu B/kT) - \text{EXP}(-\mu B/kT)}{\text{EXP}(\mu B/kT) + \text{EXP}(-\mu B/kT)}$$

where μ is the proton magnetic moment, B is the strength of the static external field, k is the Boltzman constant and T is the equilibrium temperature. P_{thermal} thus

depends critically on an accurate knowledge of the temperature which appears inversely in the exponential factor. Measurement of the equilibrium temperature and in particular the electron spin temperature is difficult as the lattice temperature must be determined indirectly by monitoring vapor pressure in the cryostat.⁵ Uncertainty in the temperature calculation introduces a systematic error into the overall NMR measurement.

A second experimental difficulty is associated with the weak thermal equilibrium signal which was the order of 0.1% of the enhanced signal. Distortions arising from electronic amplification and noise are much more serious for the small thermal signal, particularly as the nuclear signal appears as a small a.c. modulation on a large d.c. offset.

A further limiting aspect of the NMR measurement is that all parts of the sample contribute equally to the measurement. Inhomogenieties in the magnetic field and surface effects in the sample cause local variations in the Larmor precessional frequency of the protons. The signal is an average over the entire volume of the sample. In comparison the nuclear scattering measurement samples only those protons in the target that contribute to scattering. Hence this method is more direct in giving information on the initial spin state of those protons which interact via a spin dependent potential in the

fundamental process being studied (i.e. $\Delta\sigma_L$).

Consequently all systematic errors are estimated to limit the overall accuracy of the NMR measurement to the order of 6%.

The measurement of target polarization by the nuclear scattering method is limited by statistical errors since the data can be accumulated only for a finite time. This time was estimated such that the statistical errors were less than uncertainties arising from the phase shift predictions for C_{LL} and the other components of the scattering matrix which enter in the calculation. These errors were added in quadrature with the statistical errors. To these was added a small uncertainty in the angular distribution of the scattered events. The overall uncertainty obtained in this measurement was of the order of $\pm 2\%$. This measurement thus provided a calibration of the NMR system.

The formalism describing the nuclear scattering measurement is summarized in Chapter 2. The description is based on the density matrix formalism which is particularly well suited to this application. A brief discussion of dynamic nuclear orientation is given in the same chapter. Included is a description of the method used to prepare the initial polarization state for the scattering experiment. Finally Q meter detection which constituted the detection system of the NMR measuring

apparatus employed in this experiment is described.

A general description of beam line apparatus and essential equipment including the polarized target and NMR apparatus is given in Chapter 3. Chapter 4 is devoted entirely to a description of the polarization monitor which was used to observe the nuclear scattering. In Chapter 5 a short account of the procedure for recording experimental data is given. The duration of the experiment was one week hence only some general aspects of the data acquisition program are included.

Details of the analysis used to obtain the target polarization are summarized in Chapter 6. Track reconstruction of protons scattered into the monitor is described. The reconstructed trajectories were used to compute the coplanar and opening angle for each scattering event. Use of a coplanarity test to separate elastic two body events in hydrogen from background scattering is described. The fitting equation used to obtain the target polarization are presented and discussed. Finally the calculation of an overall uncertainty in the measurement is described.

The results of the nuclear scattering measurement with error analysis and conclusion are presented in the final Chapter.

Chapter II

FORMALISM

This Chapter gives a description of the density matrix formalism in nucleon-nucleon scattering, the methods of dynamic nuclear orientation and the technique of Q-meter detection

2.1 The Scattering Matrix

The kinematics of elastic proton proton scattering are completely determined by two parameters, which may be chosen as the centre of mass momentum, k , of the incident proton and the centre of mass scattering angle $\theta_{c.m.}$. The spin dependence of the interaction has been conveniently formulated in a matrix representation.⁶ In this formalism the scattering amplitudes, $f(k, \theta_{c.m.})$, for each possible spin configuration are the components of a matrix. The initial spin state n is specified by a four component vector $x^{(n)}$. In the asymptotic limit as r becomes much larger than the range of the interaction the wave function of the scattered particle is given by

$$\psi^{(n)} = e^{i\mathbf{k} \cdot \mathbf{r}} X^{(n)} + f^{(n)} \frac{e^{ikr}}{r}$$

where

$$f^{(n)} = MX^{(n)} \quad (2.1)$$

M is a 4x4 matrix which is a function of k , $\theta_{c.m.}$ and the Pauli spin operators, $\sigma^{(1)}$ and $\sigma^{(2)}$, for the two particles.

The incident momentum vector \mathbf{k} and the scattered momentum vector \mathbf{k}' are used to define three orthonormal cartesian vectors in the c.m. frame given by

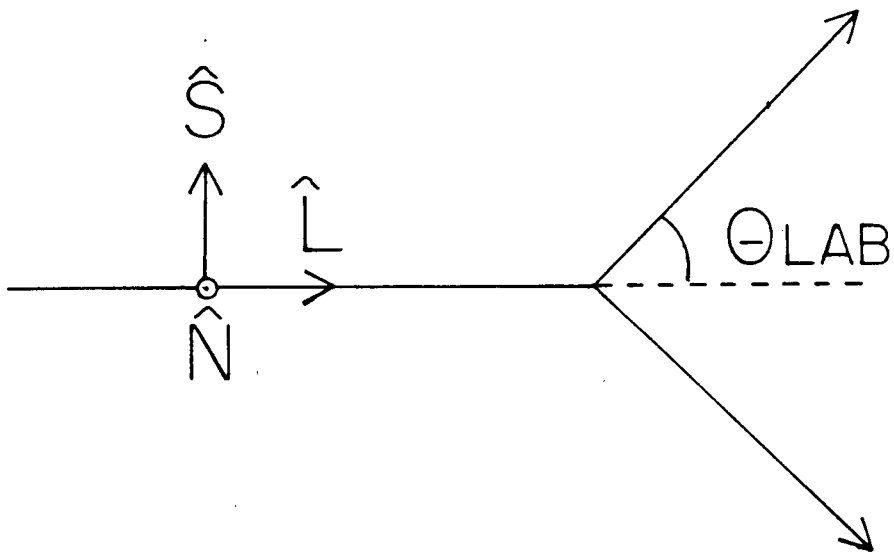
$$\hat{P} = \frac{\mathbf{k} + \mathbf{k}'}{|\mathbf{k} + \mathbf{k}'|}, \quad \hat{N} = \frac{\mathbf{k} \times \mathbf{k}'}{|\mathbf{k} \times \mathbf{k}'|}, \quad \hat{K} = \frac{\mathbf{k} - \mathbf{k}'}{|\mathbf{k} - \mathbf{k}'|} = \hat{N} \times \hat{P} \quad (2.2)$$

The most general form of M that preserves invariance under space rotations, reflections and time reversal is

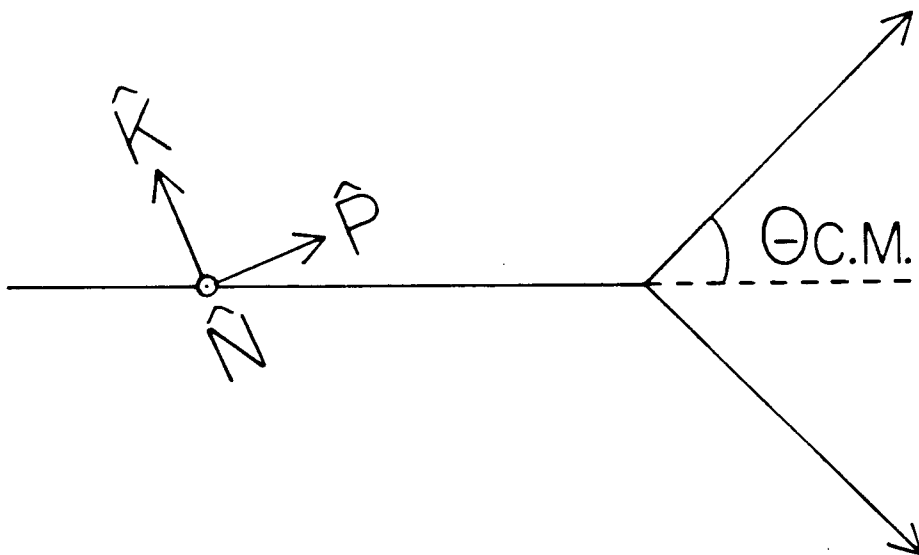
$$\begin{aligned} M = & a + c(\sigma_N^{(1)} + \sigma_N^{(2)}) + m(\sigma_N^{(1)} \sigma_N^{(2)}) \\ & + g(\sigma_P^{(1)} \sigma_P^{(2)} + \sigma_K^{(1)} \sigma_K^{(2)}) + h(\sigma_P^{(1)} \sigma_P^{(2)} - \sigma_K^{(1)} \sigma_K^{(2)}) \end{aligned} \quad (2.3)$$

where the subscripts k, N , and P indicate the direction of the spin vector with respect to the definitions in 2.2. The coefficients a, c, m, g and h are known as the amplitude of the scattering matrix. The spin scattering matrix M is related to the scattering matrix S by

$$M = \frac{2\pi}{iP} \langle \theta_f \phi_f | s-1 | \theta_i \phi_i \rangle \quad (2.4)$$



LABRATORY FRAME



C.M. FRAME

FIGURE 2.1
KINEMATIC DIAGRAM

where the bra and ket vectors specify the direction of motion of the outgoing and incoming nucleons whose relative momentum is described by wave number p .

The matrix M is used in the framework of a density matrix formalism⁷ to relate the initial spin state of two scattering nucleons to the expectation value of the spins in the final state given by

$$\langle \sigma_{\alpha}^{(1)} \sigma_{\beta}^{(2)} \rangle_f \quad (\alpha, \beta = 0, 1, 2, 3) \quad (2.5)$$

where $\sigma_0 = 1$ corresponds to a measurement where the spin component is not determined and 1, 2 and 3 correspond to the direction \hat{P}, \hat{N} and \hat{k} . For a pure spin state $\chi^{(n)}$, the density matrix is defined as

$$\rho_{ij} = \chi_i^{(n)} \chi_j^{(n)\dagger} \quad (2.6)$$

where $\chi_i^{(n)}$ is the i th component of the column vector $\chi^{(n)}$ and $\chi^{(n)\dagger}$ is the adjoint row vector. For an incoherent mixture of pure spin states as is a beam produced by an accelerator, the density matrix is defined

$$\rho_{ij} = \sum_n p_n \chi_i^{(n)} \chi_j^{(n)\dagger} \quad (2.7)$$

where p_n is the probability of finding the system in state $\chi^{(n)}$. The expectation value $\langle s^{(\mu)} \rangle$ of any spin operator $s^{(\mu)}$ is

$$\begin{aligned} \langle s^{(\mu)} \rangle &= \frac{\sum_n p_n (\chi^{(n)}, s^{(\mu)} \chi^{(n)})}{\sum_n p_n (\chi^{(n)}, \chi^{(n)})} = \frac{\sum_n \sum_{ij} p_n \chi_i^{(n)\dagger} s_{ij}^{(\mu)} \chi_j^{(n)}}{\sum_n \sum_{ij} p_n \chi_i^{(n)\dagger} \chi_j^{(n)}} \\ &= \frac{\text{Tr}(\rho_f s^{(\mu)})}{\text{Tr}(\rho_f)} \end{aligned} \quad (2.8)$$

Hence

$$\langle \sigma_{\alpha}^{(1)} \sigma_{\beta}^{(2)} \rangle_f = \frac{\text{Tr}(\rho_f \sigma_{\alpha}^{(1)} \sigma_{\beta}^{(2)})}{\text{Tr}(\rho_f)} \quad (2.9)$$

The final state density matrix ρ_f is expressed in terms of the matrix M and the density matrix ρ_i , which describes the preparation of the initial state. From 2.1

$$\rho_f = \sum_n P_n M \chi^{(n)} \chi^{(n)\dagger} M^{\dagger} = M \rho_i M^{\dagger} \quad (2.10)$$

and the final state expectation value of spin is

$$\langle \sigma_{\alpha}^{(1)} \sigma_{\beta}^{(2)} \rangle_f = \frac{\text{Tr}(M \rho_i M^{\dagger} \sigma_{\alpha}^{(1)} \sigma_{\beta}^{(2)})}{\text{Tr}(M \rho_i M^{\dagger})} \quad (2.11)$$

Defining $S^{(\mu)} = \sigma_{\alpha}^{(1)} \sigma_{\beta}^{(2)}$, $\mu = 1, 2, \dots, 16$, the relation between initial and final polarization states is

$$I \langle S^{(\mu)} \rangle_f = \frac{1}{4} \sum_{\nu=1}^{16} \langle S^{(\nu)} \rangle_i \text{Tr}(M S^{(\nu)} M^{\dagger} S^{(\mu)}) \quad (2.12)$$

where I is the differential scattering crosssection from the initial state $|\theta_i \phi_i\rangle$ into the final state $\langle \theta_f \phi_f|$.

For experimental convenience the reference frame is re-defined to be the laboratory coordinate system. The crosssection, $I_{\alpha\beta}$, corresponding to a measurement where a polarized beam with polarization along α scatters from a polarized target with polarization along β , and the final polarizations are not observed, is written

$$\begin{aligned} I_{\alpha\beta} &= \frac{1}{4} \text{Tr}(M M^{\dagger}) \\ &+ \frac{1}{4} \text{Tr}(M \sigma_{\alpha}^{(1)} M^{\dagger}) \langle \sigma_{\alpha}^{(1)} \rangle_i + \frac{1}{4} \text{Tr}(M \sigma_{\beta}^{(2)} M^{\dagger}) \langle \sigma_{\beta}^{(2)} \rangle_i \\ &+ \frac{1}{4} \text{Tr}(M \sigma_{\alpha}^{(1)} \sigma_{\beta}^{(2)} M^{\dagger}) \langle \sigma_{\alpha}^{(1)} \rangle_i \langle \sigma_{\beta}^{(2)} \rangle_i \end{aligned} \quad (2.13)$$

The first term is I_0 , the differential crossection for scattering of an unpolarized beam from an unpolarized target and the next two terms are the polarization $I_0 P$. By defining a tensor $C_{\alpha\beta}$ such that

$$I_0 C_{\alpha\beta} = \frac{1}{4} \text{Tr} (M \sigma_{\alpha}^{(1)} \sigma_{\beta}^{(2)} M^{\dagger}) \quad (2.14)$$

equation 2.13 takes on the form

$$\begin{aligned} I_{\alpha\beta} = I_0 \{ & 1 + P (\delta_{\alpha N} \langle \sigma_{\alpha}^{(1)} \rangle_i + \delta_{\beta N} \langle \sigma_{\beta}^{(2)} \rangle_i) \\ & + C_{\alpha\beta} \langle \sigma_{\alpha}^{(1)} \rangle_i \langle \sigma_{\beta}^{(2)} \rangle_i \} \end{aligned} \quad (2.15)$$

where δ is the Kronecker delta. $\langle \sigma_{\alpha}^{(1)} \rangle_i$ is the expectation value of the beam spin along α in the initial state and $\langle \sigma_{\beta}^{(2)} \rangle_i$ is the expectation value of the target spin along β in the initial state (i.e. the components of beam and target polarization). The dependence of the scattering on the two kinematic variables is implicit in the definition of P and $C_{\alpha\beta}$ through their relation to the matrix M , whose components are the scattering amplitudes.

Numerous experiments have been done to determine the scattering matrix. The present work was not designed to contribute to that determination but rather made use of existing information on M to determine the target polarization. Equation 2.15, expressed in $\Delta\sigma_L$ configuration (eq. 6.4), was precisely the equation used to determine the target polarization. In this configuration both beam and target had zero component of polarization

in the normal direction. Hence the second term of 2.15 did not contribute to scattering and is absent in 6.4. The components of the tensor $C_{\alpha\beta}$ which did contribute were C_{LL} , C_{SS} and C_{SL} . The contribution of the C_{SS} and C_{SL} terms resulted because both the beam and the target spins had a non zero component in the sideways direction. The origin of these non-longitudinal components is explained in the discussion on apparatus given in Chapters three and four.

2.2 Dynamic Nuclear Orientation

Some of the basic concepts involved in the preparation of an initial polarization state are described in this section, beginning with a description of the fundamental principles of nuclear orientation.

The magnetic dipole moment vector $\underline{\mu}$, of a particle or atom is related to its angular momentum vector \underline{I} by the expression

$$\underline{\mu} = g \beta \underline{I} \quad (2.16)$$

where β is the Bohr magneton and g is the g -factor appropriate to the system being considered. The interaction energy of the dipole moment with a magnetic field \underline{H}_0 is

$$E = - \underline{\mu} \cdot \underline{H}_0 \quad (2.17)$$

The dipole exists in discrete energy levels given by

$$E_m = g\beta m H_0 \quad (2.18)$$

Each level is characterized by m , the expectation value of the spin component in the direction of the applied field. For an assembly of identical dipoles in equilibrium at a temperature $T(^{\circ}\text{K})$, the relative number, N_m , of the whole assembly in state m is given by the Boltzman equation

$$N_m = \text{EXP}(-E_m/kT) \quad (2.19)$$

When the temperature is sufficiently low that the magnetic energy is larger than the random thermal energy, the number of dipoles with spins aligned parallel to the field, N_+ , exceeds the number with spins aligned anti-parallel N_- . The spins are preferentially oriented and a suitable measure of this polarization P , is given by

$$P = \frac{1}{I} \frac{\sum_{m=-I}^I m N_m}{\sum_{m=-I}^I N_m} \quad (2.20)$$

The magnetic properties of the assembly can be described by the magnetisation M , defined by

$$M = Ng\beta \frac{\sum_{m=-I}^I m \text{EXP}(g\beta m H_0/kT)}{\sum_{m=-I}^I \text{EXP}(g\beta m H_0/kT)} \quad (2.21)$$

where N is the total number of dipoles in the assembly

The exponential factors appearing in the definition of M are N_m as given by 2.19. Therefore the magnetisation is simply related to the polarization by

$$M = Ng\beta IP \quad (2.22)$$

At a temperature of approximately 1°K and a field of 25 KG the electrons in the paramagnetic ions are essentially 100% polarized but the nuclear spin states are essentially equally populated except for the small Boltzman factor which leads to proton polarizations of the order of 0.5%.

The proton polarization can be enhanced by dynamic methods. The important features of dynamic polarization can be illustrated in a simple model. In this model the sample is an assembly of paramagnetic ions each in a hyperfine coupling with the free protons. The sample is placed in a microwave cavity at liquid He temperature and in a strong external field. Denoting the electron magnetic quantum number S and nuclear spin projection m , the energy levels of the system are

$$E(s,m) \approx g\beta H_0 S + A s m \quad (2.23)$$

Here g is the electronic spectroscopic splitting factor and A takes on a value such that the hfs interaction is secondary but still much larger than the interaction of the proton spin directly with the external field, which is neglected. The splittings of the levels in units of kT

(Figure 2.2) are

$$\delta = A/2kT \text{ and } \Delta = g\beta H_0/kT \quad (2.24)$$

The labelling of states in Figure 2.2 corresponds to the electronic and nuclear spin projections. For example, $(++)$ means $(S=+\frac{1}{2}, m=+\frac{1}{2})$ etc.

Dynamic nuclear polarization is achieved by connecting an rf oscillator to the cavity containing the sample. With the oscillator frequency set such that $h\nu = g\beta H_0$, transition between the states $(+-)$ and $(-+)$ are induced. This transition corresponds to flipping the electron spins up and the nuclear spins down. The populations of these two levels will eventually become equal since rf induced emission and absorption rates are equal. Assuming $N_{+-} = N_{-+} = 1$, the relative population of the other two levels will be determined by the relevant relaxation mechanism. As the dominant mechanism favors transitions where $\Delta s=1$ and $\Delta m=0$, the steady state populations tend to

$$\frac{N_{++}}{N_{-+}} = e^{-\Delta - \delta} \text{ and } \frac{N_{+-}}{N_{--}} = \frac{1}{e^{\Delta - \delta}} \quad (2.25)$$

resulting in dynamic nuclear polarization of the system approximately equal to $-\Delta/2$. Now if the oscillator is set to induce transitions between the states $(--)$ and $(++)$ the relaxation mechanism will establish a steady state polarization of $+\Delta/2$.

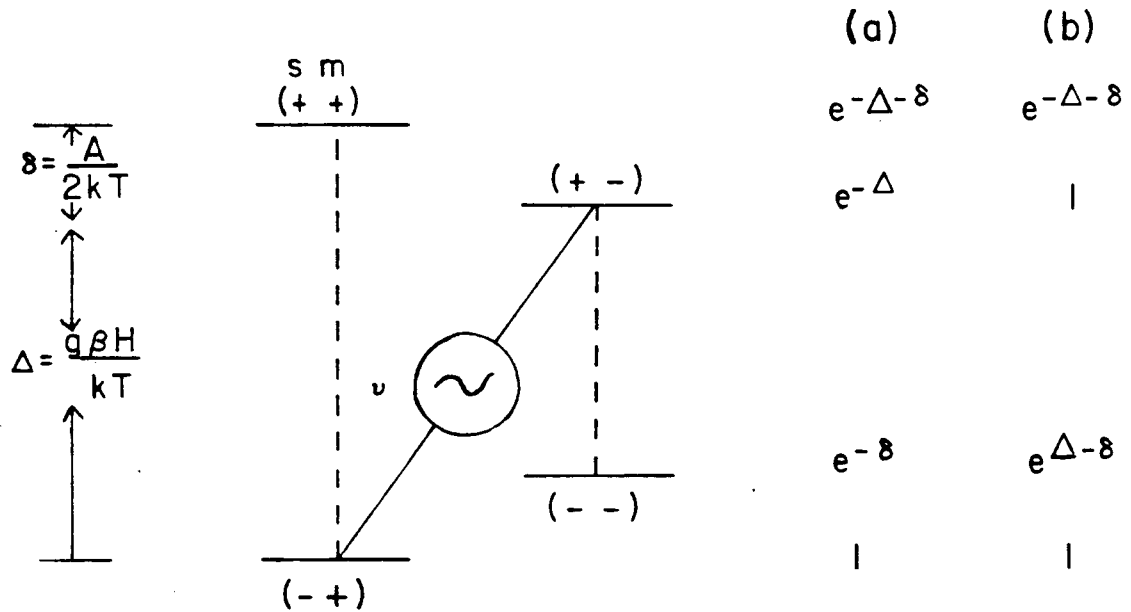


FIGURE 2.2 ENERGY LEVEL DIAGRAM

column (a) gives the relative populations at thermal equilibrium; column (b) gives the dynamic equilibrium populations achieved by r.f. saturation of the transition shown

2.3 Q-Meter Detection

The NMR measuring apparatus used in this experiment detected nuclear orientations by a simple method known as Q-meter detection. This method exploits some of the well known properties of rf coils which will be reviewed briefly in this section.

A current i circulating in the coil produces a magnetic field \underline{H} linearly polarized along the axis of the coil. The magnetic flux across the coil due to this current is

$$\Phi = Li \quad (2.26)$$

where L is the coil inductance. For a current with time dependence given by

$$i = \text{Re} \{ I e^{j\omega t} \} \quad (2.27)$$

The quality factor Q , of the coil is defined

$$P = W\omega/Q \quad (2.28)$$

where $P = \frac{1}{2} I^2 r$ is the power dissipated in the coil of resistance r , and $W = \frac{1}{2} L I^2$ is the maximum energy stored in the coil. Equivalently Q can be written

$$Q = L\omega/r \quad (2.29)$$

The coil is arranged such that the rf field is perpendicular to a uniform external field H_0 . Thus the

nuclear magnetisation is forced to precess about H_0 by the driving rf field. The magnetisation has a component, $M_{//}$, along the rf field direction equal to

$$M_{//} = \text{Re} \{ 2\chi_{\text{He}} e^{j\omega t} \} \quad (2.30)$$

inside the sample and zero outside. The complex rf susceptibility, χ , can be written as $\chi' - j\chi''$ and is vanishingly small except at resonance. The flux at the induction vector, $\underline{B} = \underline{H} + 4\pi\underline{M}$, across the coil is

$$B = \text{Re} \{ L(1+4\pi\chi\eta) I e^{j\omega t} \} \quad (2.31)$$

where η is the sample filling factor. This is equivalent to saying that in the presence of nuclear magnetisation the inductance takes on the complex values $L(1+4\pi\chi\eta)$.

When a capacitance C is added in series with the coil containing the sample and the circuit is driven by a constant current generator it develops a voltage across its terminals proportional to its series impedance Z , given by

$$Z = r + j \left(\omega L(1+4\pi\chi\eta) - \frac{1}{\omega C} \right) \quad (2.32)$$

When the rf field is swept through the resonant frequency, excitation of dipole transitions in the sample causes power to be absorbed from the coil. This absorption changes the impedance of the circuit and results in a fractional change in voltage across the circuit proportional to

$$4\pi \eta Q \chi'' \quad (2.33)$$

χ'' is related to χ_0 , the static Curie susceptibility, via dispersion relations⁸ and since the nuclear magnetisation is proportional to χ_0 ⁹, the recorded signal amplitude is proportional to the nuclear polarization. For positive polarization power is transmitted to the coil by the nuclear spins resulting in a fractional change in voltage of the opposite sign.

Chapter III

APPARATUS

Beam line 4C at TRIUMF was designed specifically for the transmission of a polarized proton beam to the polarized proton target. This description of apparatus begins with various components that can be termed beam line apparatus and includes the polarized target and NMR system.

3.1 Polarimeter

A polarimeter, previously calibrated to an accuracy of $\pm 1.5\%^{10}$, was used to measure beam polarization and monitor beam intensity. This device is a four arm telescope which measured the left-right asymmetry in beam scattered from a 50 μm thick CH_2 target suspended in the beam pipe. Each arm consisted of two plastic scintillators accurately aligned. The forward arms were positioned at 26° with respect to the beam and the recoil arms were at the conjugate angle of 60° . For proton proton elastic scattering with the incident beam polarized vertically and the target unpolarized, the polarization, denoted P_b ,

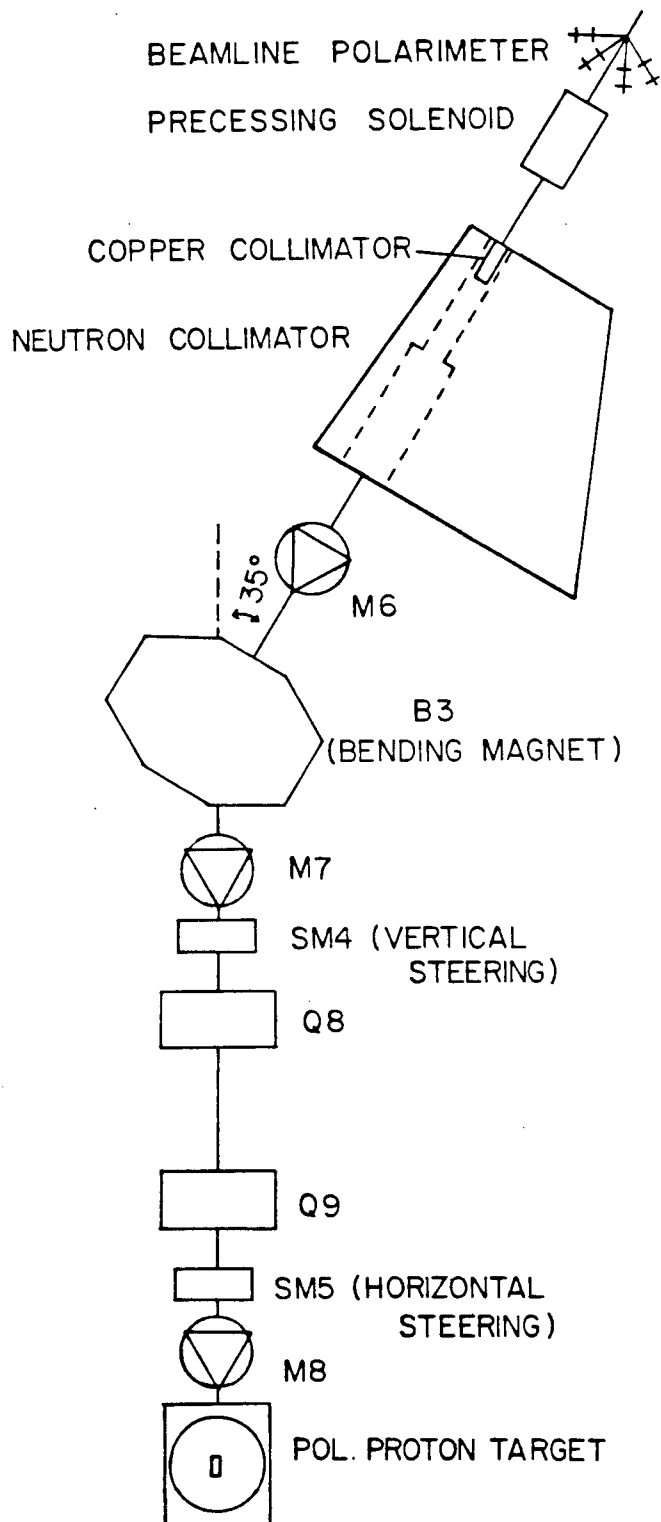


FIGURE 3.1
BEAMLINE 4C

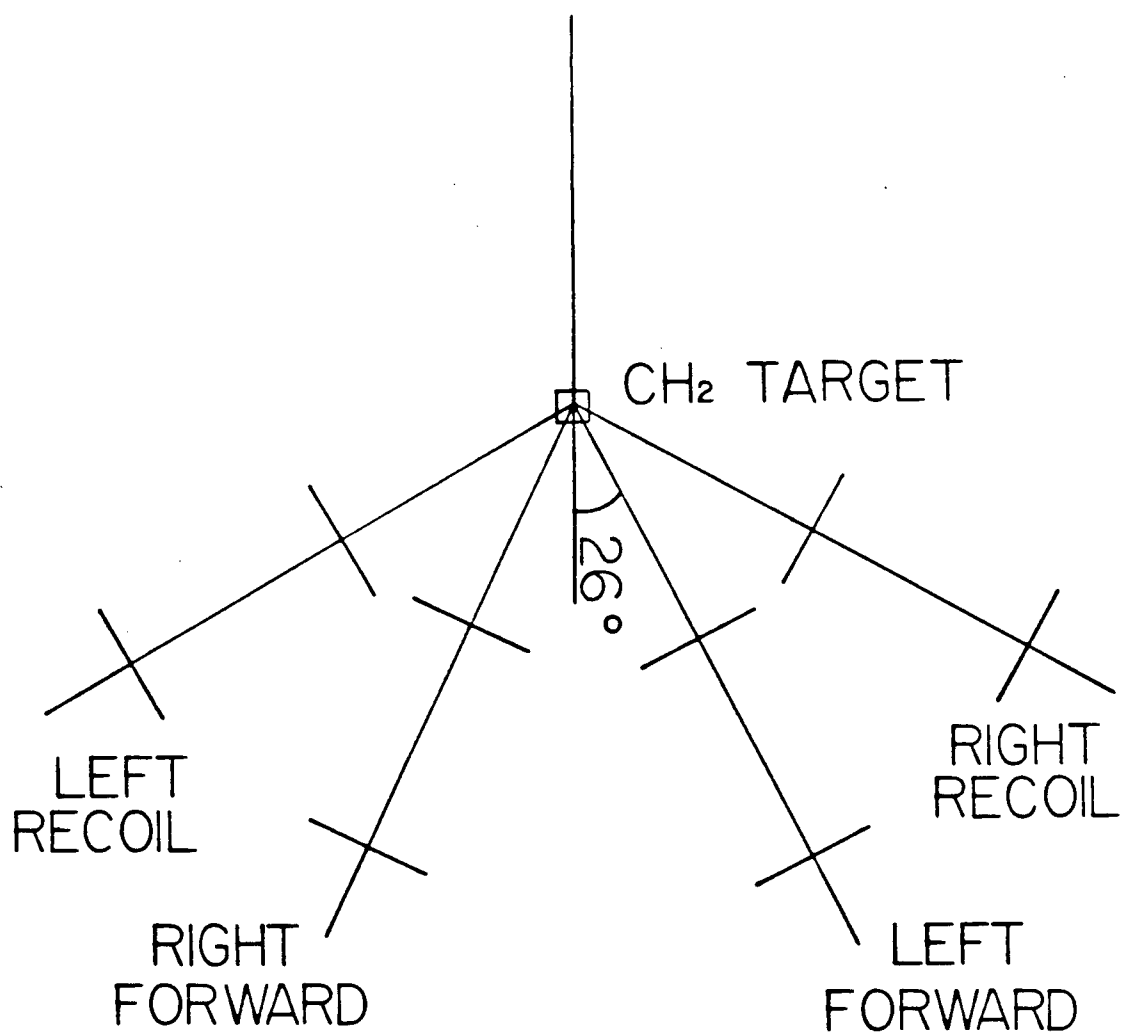


FIGURE 3.2

BEAMLINER POLARIMETER

is related to the scattering asymmetry ϵ by

$$P_b = \epsilon/P$$

where ϵ is defined

$$\epsilon = \frac{\# \text{Left} - \# \text{Right}}{\# \text{Left} + \# \text{Right}}$$

The polarization parameter P has been accurately measured in a previous experiment.¹⁰ The correction rates for the carbon content of the target have also been determined in the same experiment.

3.2 Super Conducting Solenoid

The TRIUMF cyclotron produces beam polarized in the vertical direction. In this experiment the proton spins were precessed in two stages to the longitudinal. The first precession through 90° into the sideways direction was performed by a super conducting solenoid. The solenoid used was 1m long with a 10 cm warm bore. It is capable of producing a uniform 6 tesla magnetic field when operated at the maximum rated current of 212A. The line integral of the magnetic field along the axis of the solenoid was calculated to be $0.028187 \text{ T-M-A}^{-1}$.

The precession angle of the spin vector in a uniform magnetic field B was calculated using the

$$\alpha = \frac{e\hbar}{p} \int \underline{B} \times \underline{d\ell}$$

where e is the proton charge, P is its momentum and μ is the proton magnetic moment. The solenoid currents calculated to effect a 90° precession are given in Table 3.1.

3.3 Collimator

A collimator of approximately 30 cm thickness and 3.5 m in length followed the solenoid. The collimator was constructed from 2 steel plates 50 mm thick and filled with lead. It was originally designed for use in neutron experiments. There are 11 equally spaced ports from -3° to $+27^\circ$, each port having an up stream diameter of 10 cm and a down stream diameter of 12.5 cm. This experiment utilized only the 0° port. A 20 cm. long copper plug with 1mm bore was inserted in the 0° port. The plug was used to reduce the beam intensity to the level of 10^5 to 10^6 required for this experiment.

3.4 4B3 Bending Magnet

This dipole magnet performed two functions. First it was used to deflect the collimated beam through a 35° bend in the beam line on its way to the experimental area. This angle is approximately optimum for precessing proton spins from the sideways to the longitudinal direction at TRIUMF energies. The amount of deflection was calculated from the expression

Table 3.1

Solenoid Currents Calculated to Effect a 90° Precession

<u>ENERGY</u>	<u>CURRENT (A)</u>
519.9	74.25
500.7	72.50
459.4	68.95
423.3	65.78
329.6	56.26
208.2	44.03

Table 3.2

Currents in the Bending Magnet Calculated for a 35° Bend

<u>ENERGY</u>	<u>CURRENT (A)</u>
519.9	2295.0
500.7	2205.0
459.4	1995.0
423.3	1833.0
329.6	1500.0
208.2	1131.0

$$\theta = \frac{e}{p} \int \underline{B} \times \underline{d\ell}$$

where θ is in radians. The currents needed to deflect the incident protons through 35° were calculated for each of the experimental energies and are tabulated in Table 3.2.

Secondly, protons which had suffered energy loss in the collimator were deflected at angles greater than 35° . They were effectively swept out of the beam by the field. This resulted in the selection of a narrow momentum bite.

In coming through the bending magnet the proton spins were precessed not exactly to the longitudinal, but by an amount w.r.t. the sideways direction given by

$$\psi = \mu \gamma \theta$$

where

$$\gamma = \left(\frac{E}{M}\right)_{\text{protons}}$$

The resulting sideways component of the spin vector, given by $\cos(\psi)$ is responsible in part for the contribution of the C_{sL} component of the tensor $C_{\alpha\beta}$ to the cross section in 2.15.

3.5 Quadrupole and Steering Magnets

A vertical steering magnet, two quadrupole focussing magnets and a horizontal steering magnet were placed in succession down stream of the bending magnet. In this experiment the quadrupole magnets were not used as the beam properties were found to be acceptable without

them. The steering magnets each have a pole gap of 100 mm and a maximum rated current of $\pm 7A$. They were used to centre the beam on the target.

3.6 Monitor 4CM8

Monitor 4CM8 was used to check beam focus and centering approximately 1m upstream from the target. It was permanently installed in the beam line and evacuated by the beam line vacuum system. The monitor consisted of an aluminum outer casing housing a multi wire proportional chamber. The monitor was swung into the beam path to obtain a beam profile, then swung aside.

3.7 Polarized Target Cell

The target cell was a poly tetra fluoro ethylene (teflon) cylinder measuring 2.4 cm (length) by 1.5 cm (diameter). The target composition was, by weight, 95% $C_4H_{10}O$ and 5% H_2O doped with 2-ethyl-2hydroxybutyric acid - Cr(v) Complex (i.e. EHBA-Cr(v)). The target material was frozen into beads 1.0 to 1.7 mm in diameter. The density of free hydrogen in the target, determined from three weighings of the target material and measurements of the cell volume, was $0.0765 \pm 0.0003 \text{ gm/cm}^3$. On operating, temperature of 500 millikelvin was produced by a ^3He evaporation refrigerator, designed and previously used at Liverpool University. Proton spin alignment was achieved in a field of 25 KG produced by a pair of superconducting

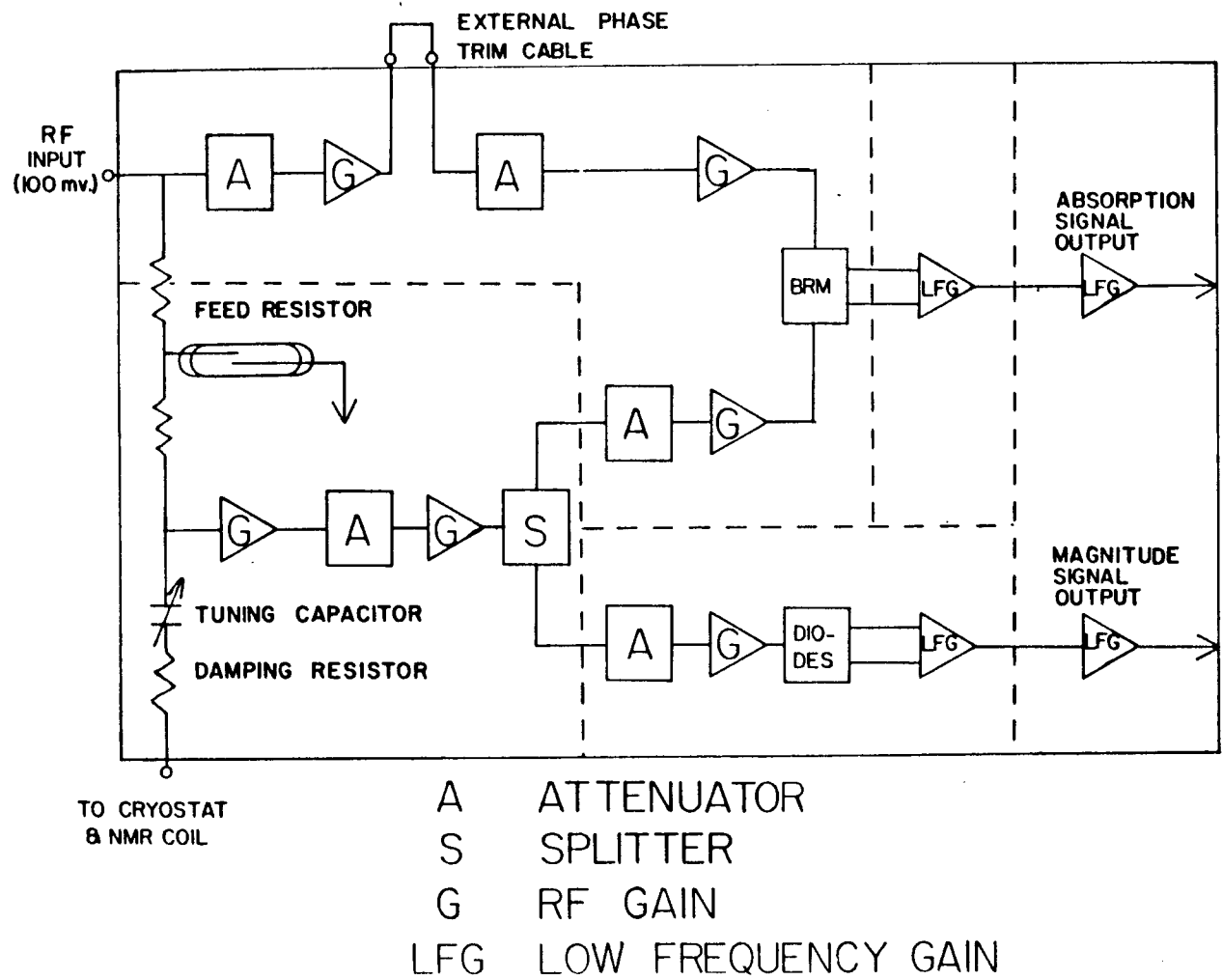


FIGURE 3.3
NMR FUNCTIONAL DIAGRAM

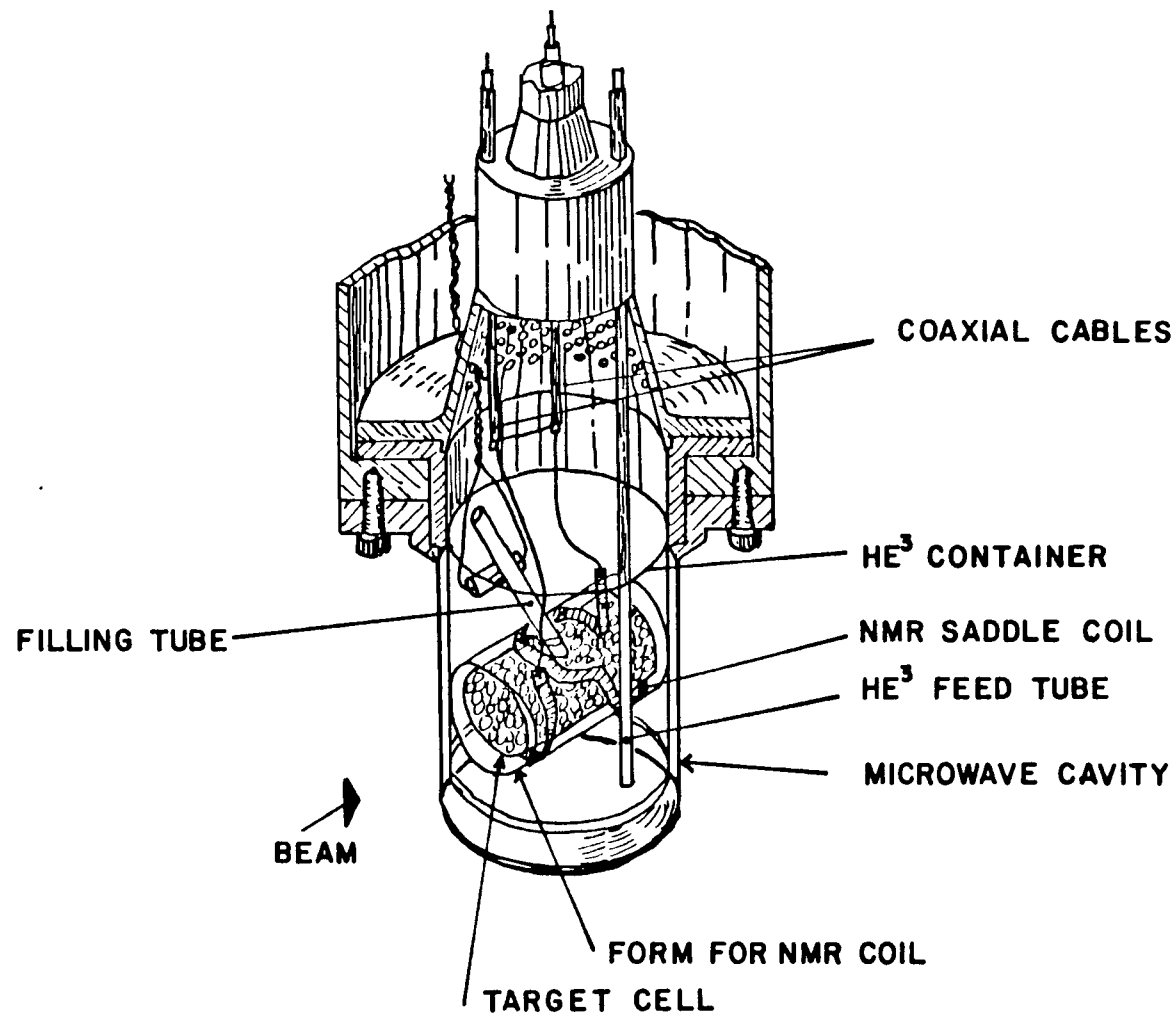


FIGURE 3.4 SCHEMATIC OF THE CRYOSTAT

Helmholtz coils. A Klystron operated in the neighbourhood of 71 GHz enhanced target polarization with spin flips accomplished by adjusting the frequency.

3.8 NMR System

A saddle coil wrapped around a teflon form containing the target cell formed the inductive element of a series tuned LRC circuit. The saddle coil was constructed from 0.05 mm thick copper foil and satisfied the requirement that the rf field direction should be perpendicular to the static field direction. Radio frequency power was supplied by a Rockland model 5600 frequency synthesizer. The rf driver was programmed to sample 301 frequencies centered on 108.8 MHz in steps of 1 KHz. The main detector employed a balanced ring modulator (BRM) operating as a full wave synchronous rectifier¹¹ to reduce measurement inaccuracies but a conventional magnitude detector was incorporated to facilitate tuning. Quality factor curves sampled slightly off resonance (by adjusting the static magnetic field) were digitized and stored in micro processor memory. NMR signal received during the experiment was digitized and subtracted from the stored Q curve by the micro processor, then integrated and written to an output register. The quantity recorded onto magnetic tape was thus the polarization integral in units of volts - KHz, where the polarization integral is the area between the two curves as shown in Figure 5.1 after the enhanced

signal has been normalized to the Q curve at two selected points as illustrated in 5.1.

Chapter IV

THE POLARIZATION MONITOR

The polarization monitor was a two arm telescope. Each arm consisted of a multiwire proportional chamber and a plastic scintillator. The positions of the chambers and scintillators were accurately measured to ± 2 mm. The forward arm subtended angles of 21.3° to 40.9° at the target center. The recoil arm viewed the target in the angular range of 43.8° to 63.1° .

The target cannister including Helmholtz coils and target cell was physically rotated through 12° in the horizontal plane. This rotation was necessary in order to monitor C_{LL} in the region of greatest sensitivity (45° c.m.) and where it is best known from phase shift analysis. The physical construction of the apparatus allowed unimpeded beam exit only to 50° on either side of an axis defined by the coils. Detection of recoil events out past 60° was accomplished by effectively offsetting the incident beam direction by the 12° rotation of the target assembly.

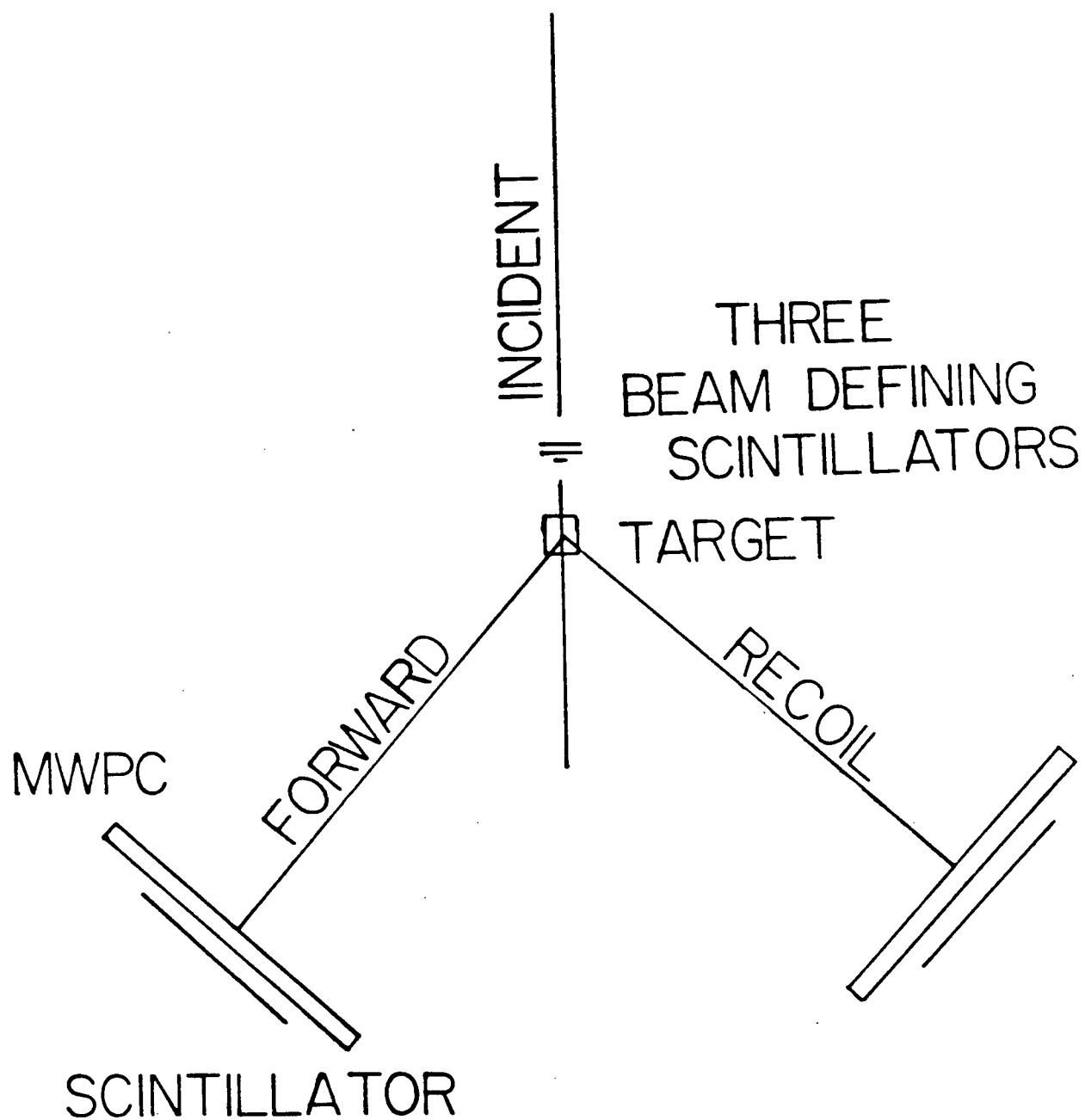


FIGURE 4.1
POLARIZATION MONITOR

Consequently the 12° rotation of the target introduced the contribution of an additional term in C_{SL} and one in C_{SS} to the cross section of 2.15. Also the rotation limited the experiment to a single coincidence telescope rather than a symmetric four armed apparatus.

The MWPC's had outer dimensions of 28.25 cm square. A magic gas mixture of 69.7% argon, 30% isobutane and .3% freon composition was continually circulated through each chamber. A plane of 1000 cathode wires spaced 2mm apart were maintained at a voltage of 4 kv. A grid of horizontal and vertical sense wires on either side of the cathode detected ion tracks produced when a charged particle passed through. Each sense plane determined two coordinates. The pulses arriving at both ends of a sense wire due to a particle track anywhere along the wire were recorded. The four pulses from each chamber were discriminated in an ECL to NIM unit and a digital pulse transmitted to a time to digital converter.

Each chamber had a scintillator placed directly behind it. The scintillators were identical with dimensions of 16.1 cm x 14.5 cm x 2 mm. The chambers were triggered on a coincidence between the three beam defining scintillators with the forward and recoil scintillators of the polarization monitor. Formally the trigger was constructed from

$S_1.S_2.S_3.L.R$

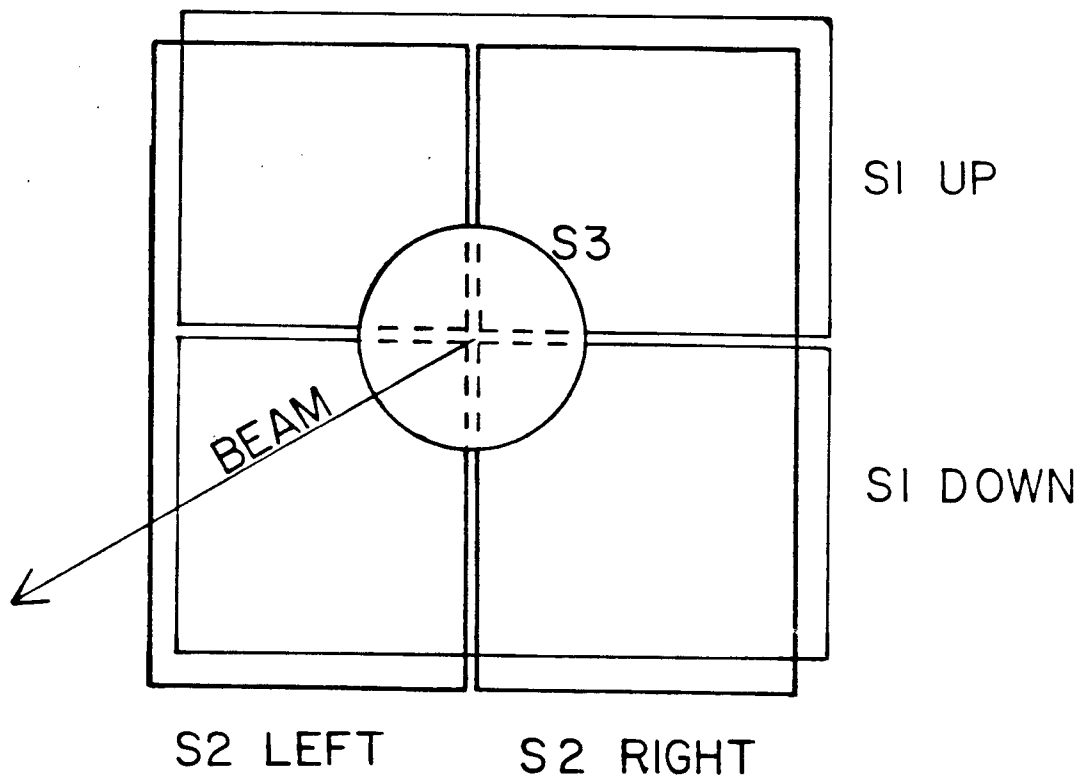


FIGURE 4.2
THREE BEAM DEFINING SCINTILLATORS

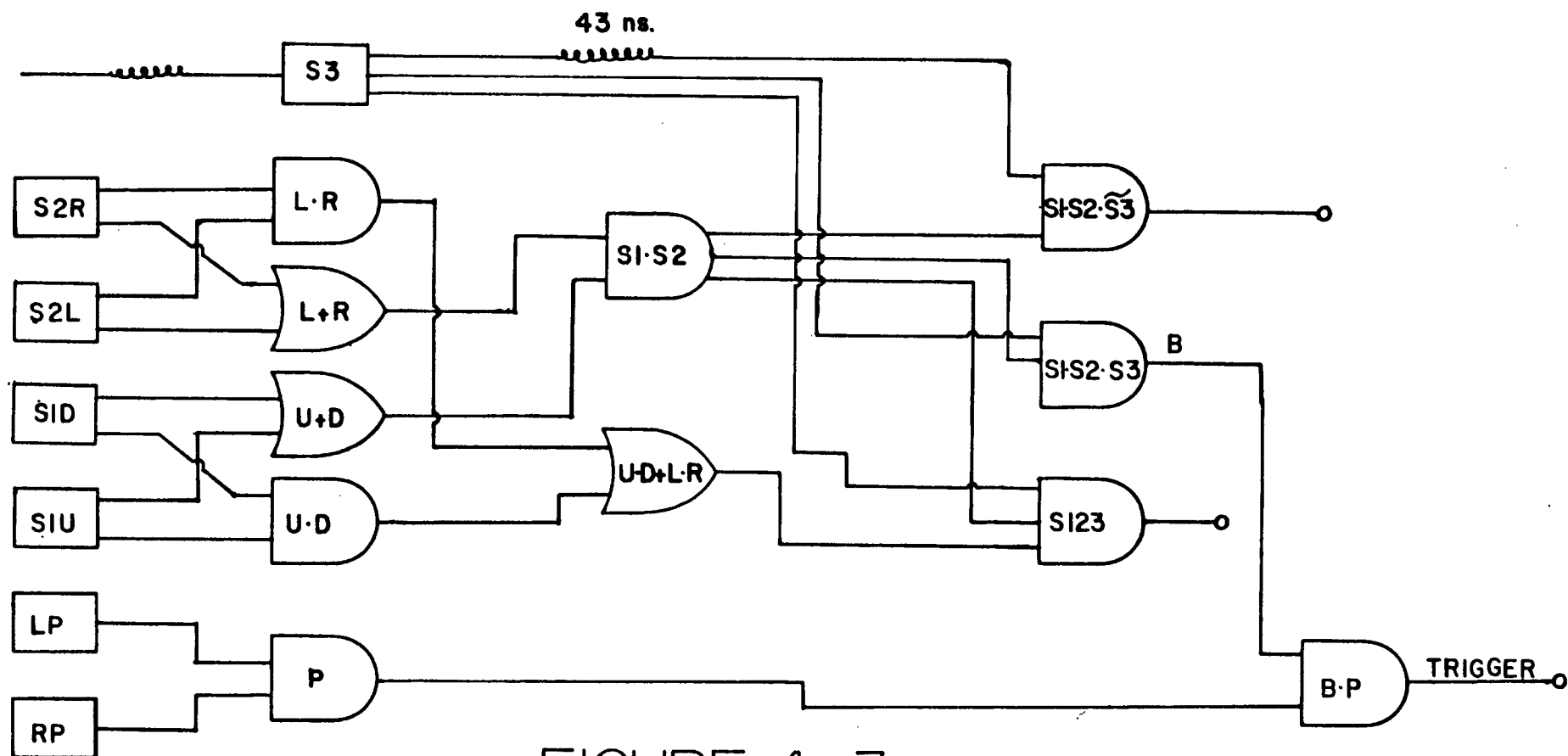


FIGURE 4.3
ELECTRONIC LOGIC DIAGRAM

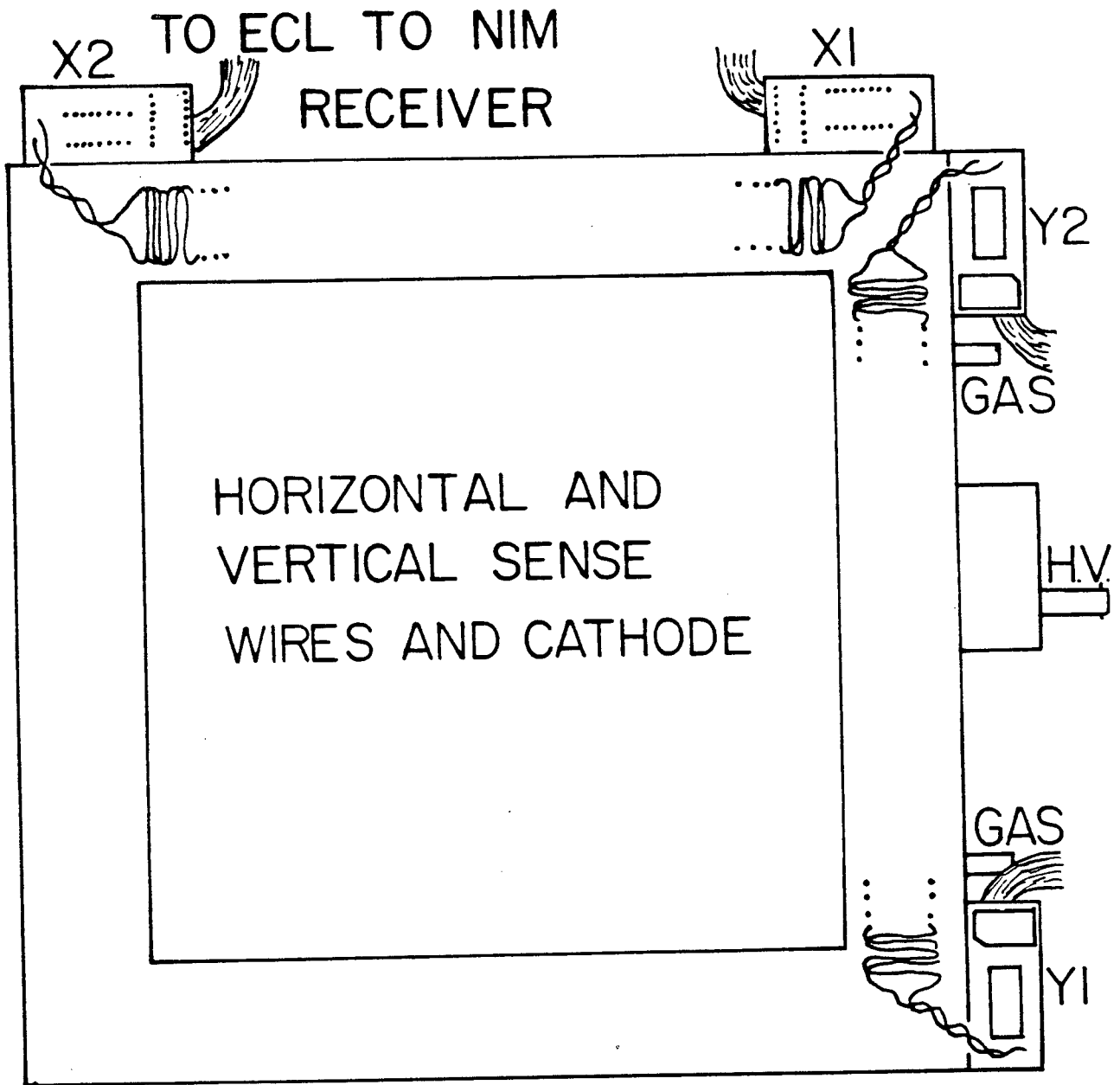


FIGURE 4.4
DIAGRAM OF A DELAY-LINE MULTI-
WIRE PROPORTIONAL CHAMBER

where s1 is an up down split scintillator, s2 is a left right split scintillator, s3 is a 1 cm in diameter circular scintillator and L,R denote the scintillators in the left and right arms of the monitor. This trigger provided a common start pulse for all the TDC's with the stop pulses coming from each of the chamber coordinates described above. The absence of a stop pulse from any chamber coordinate prompted an overflow bit to be set in the appropriate TDC. This indicator was used to determine the detection efficiency of the chambers which was defined with respect to the trigger (i.e. the trigger was assumed to be 100% efficient). The detection efficiency of each chamber was taken as the fraction of events in which pulses arrived from all four coordinates of that chamber. The detection efficiency of the monitor was taken to be the fraction of events in which the two chambers detected in coincidence an event that had produced a trigger.

The split scintillators provided a very sensitive monitor of beam stability. By monitoring the count ratio in all four quadrants a slight shift in beam position could be detected. As a precaution to guard against false asymmetries the beam spin was flipped regularly. The count ratio in the scintillators indicated no observable shift in the beam when the polarization was flipped.

Chapter V

DATA ACQUISITION

A brief description of the procedure for recording data and the preparation involved is given in this chapter. The duration of the experiment was one week.

The polarized ion source spin controller was operated in automatic spin mode giving five minutes each of spin up and spin down beam followed by one minute of unpolarized beam. The intensity of the extracted beam was monitored by the upstream polarimeter. All singles rates and useful coincidences were scaled. Scalar information along with TDC data was read through the CAMAC dataway by a PDP-11/34 computer and written onto magnetic tape. A computer generated "busy" or a "spin busy" from the spin controller formed a master inhibit, that is the scalers and TDC's were disabled while the computer was busy processing an event or when the beam polarization was being reversed. Histograms of each multiwire proportional chamber were constructed on-line and displayed on a CRT. Run times averaged 2 hours for a typical accumulation of 50,000 events.

The target polarization was reversed periodically by adjusting the klystron frequency. One half hour was required for the polarization signal to grow to its maximum. Polaroid photographs of the scope trace showing the NMR enhanced signal were made after each adjustment (see Figure 5.1).

The monitor 4CM8 was used to determine beam profiles after each new beam tune. Polaroid film exposures of the beam spot size at target entrance and exit were recorded. Steering of the beam onto the target was achieved using the vertical and horizontal steering magnets. The beam was swept through the target independently in the vertical and horizontal directions to ensure unbiased centering. Centering of the beam on the target was observed as a two percent attenuation in the transmitted beam. A plot of the attenuation during one such vertical scan is shown in Figure 5.2.

Data were taken at six extraction energies. Energy losses in transmission down the beam line were calculated. The energies of interest were those at the polarimeter and target centre, which were needed for kinematic calculations, and the energy of the beam after passing the polarimeter, which was needed to calculate precession and bend angles in the solenoid and bending magnet. There were no beam line elements directly in the path of the beam in the interval from the polarimeter to the bending magnet, hence the bend

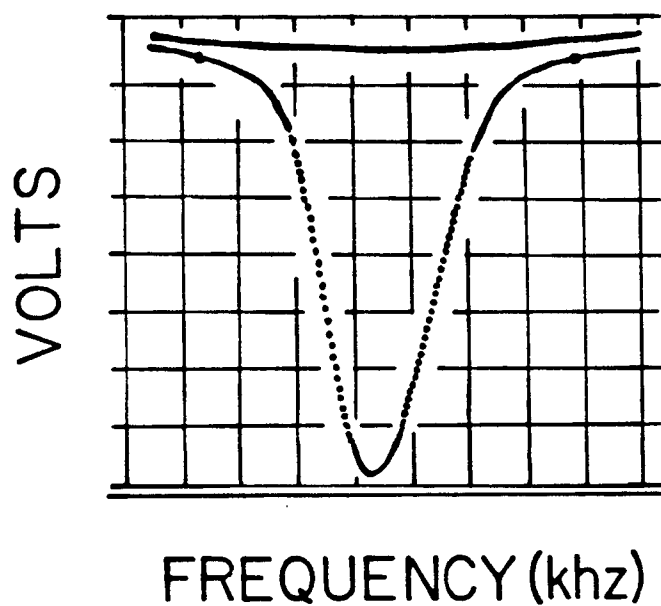


FIGURE 5.1
SCOPE TRACE SHOWING NMR SIGNAL
(REPRODUCED FROM POLAROID PHOTO)

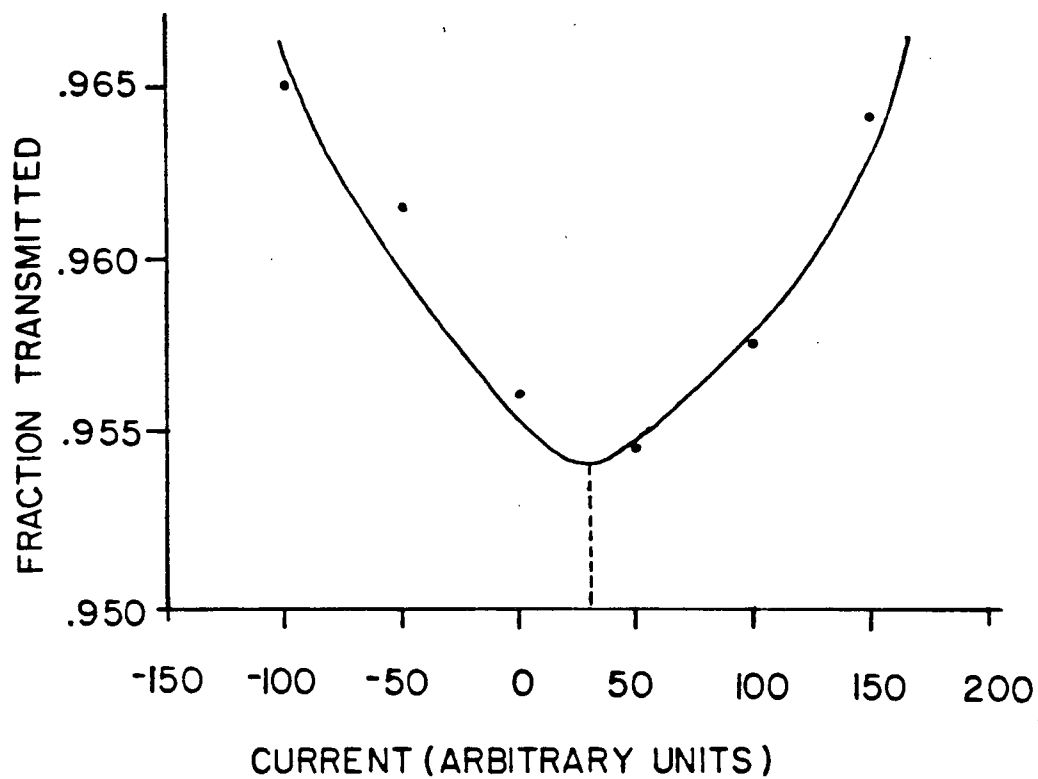


FIGURE 5.2
ATTENUATION IN BEAM TRANSMITTED
THROUGH THE TARGET

and precession angles were calculated at the same energy. These three beam energies along with the energy of the beam at extraction are given in Table 5.1.

Table 5.1

Precise Beam Energies in MeV

(at extraction, at the polarimeter, after the polarimeter, and at the target centre)

<u>Energy at Extraction</u>	<u>Energy at the Polarimeter</u>	<u>Energy After Polarimeter</u>	<u>Energy at Target</u>
520.7	520.3	519.9	516.5
501.4	501.0	500.7	497.1
460.2	459.8	459.4	455.8
424.1	423.7	423.3	419.5
330.6	330.1	329.6	325.4
209.8	209.0	208.2	202.7

Chapter VI

DATA ANALYSIS

A description of track reconstruction for protons scattered into the target polarization monitor is given at the beginning of this chapter. This chamber information was used to separate elastic hydrogen events from non elastic two body events in non hydrogenous material by a coplanarity test. The absolute target polarization was obtained from the extracted elastic data using a non linear fitting routine with chi-squared minimization.

6.1 Reconstruction of Proton Tracks

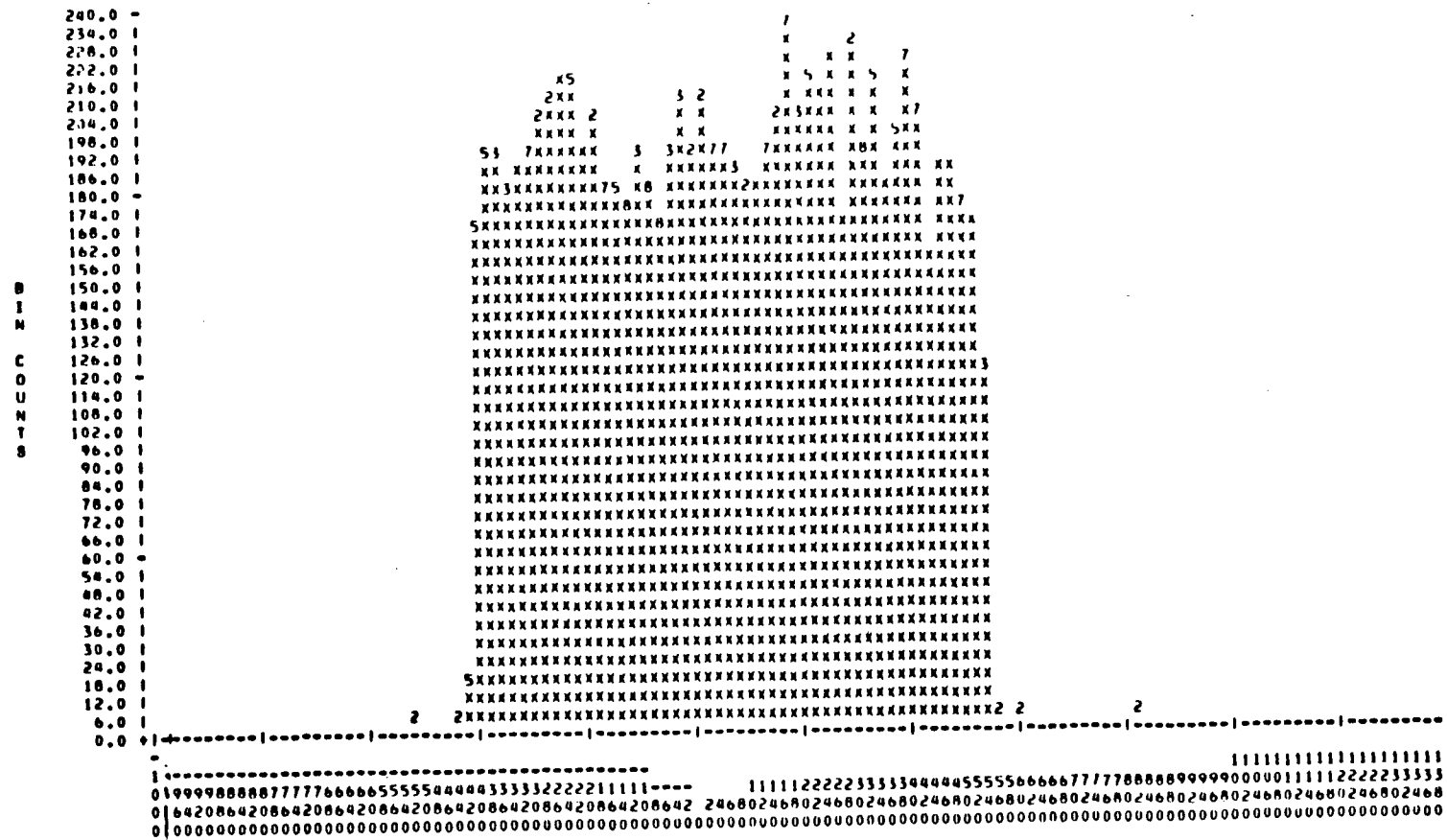
Trajectories of scattered protons were obtained by first translating the time to digital converter information into distances with respect to a cartesian coordinate system. Scattering angles were then computed with respect to this system, and corrected for deviation due to the magnetic field surrounding the polarized target.

The translation of TDC information to particle trajectories was done as follows. The chambers were of

the delay line read out type. That is the passage of a charged particle through the chamber induced a pulse on the delay line sense wire which travelled outward in both directions. The TDC digitized a time proportional to the time interval between the arrival of these pulses at either end and a common arbitrary start pulse taken to be the trigger scintillator pulse. It is the difference in the arrival time between pulses arriving at opposite ends of a chamber that determines the location of the track in the chamber. Hence common offsets in the time at both ends cancel in the computation. Location of the track with respect to the cartesian coordinate system requires determination of the correspondence between a fixed TDC channel and the coordinate system as well as the calibration of TDC channel numbers with respect to distance.

Both the calibration and reference point were obtained from histograms of the time differences mentioned above. The calibration is determined from the digital width of the distribution which is just twice the projected width of the scintillator onto the chamber as seen at the target. The histogrammed distribution is centered on the median line of the scintillator, whose coordinates were measured. Histograms were constructed for both the horizontal and vertical planes of each chamber. Thus from the chamber information the six

FIGURE 6-1 TDC DIFFERENCE HISTOGRAM



TDC SPECTRUM (DIFFERENCE)

cartesian coordinates of each proton pair triggering the monitor were calculated.

The proton tracks were deflected up to 6° by the 25 KG field required for the polarized target. The amount of deflection for each trajectory was calculated by an iterative procedure and the corrections applied to obtain the true scattering angle. Corrections were applied similarly to the incident trajectories.

In the iterative procedure, as a first approximation, the scattering angle was chosen to be the angle at which the particle had been detected. The momentum P of the scattered protons at this angle was then calculated using the following equation (derived in Appendix A) which applies to the case of a target particle at rest.

$$P(E_I^2 + m_p^2 + 2E_I m_p - P_I^2 \cos^2 \theta) + (-2P_I m_p^2 \cos \theta - 2E_I m_p P_I \cos \theta) = 0 \quad (6.1)$$

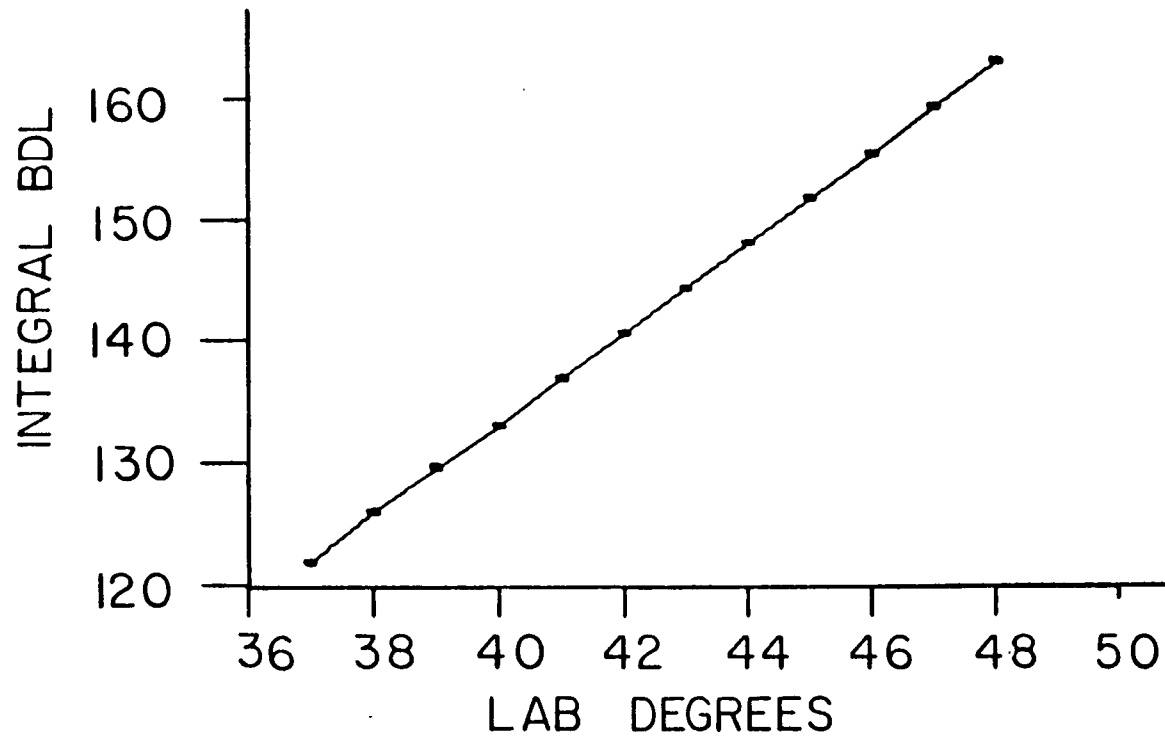
where E_I, P_I are the incident proton energy and momentum respectively and m_p is the proton mass. In each iteration the calculated momentum was corrected for magnetic deflection, using the procedure described in the following, and the computed angle compared with the observed angle. The trial scattering angle was then varied and the iteration continued till the difference between the calculated and observed angle was less than 5 milliradians.

The required properties of the magnetic field were calculated using the computer simulation routine SOL RAY, available at TRIUMF. SOL RAY simulates the magnet field produced by the Helmholtz coils of the polarized target. The field is calculated using the Biot-Savart law for a current loop, which is appropriate since the field of the Helmholtz coils is the superposition of fields from two such current loops. In the simulation, protons of definite momentum were generated at the target centre. The trajectory of each proton was followed through the magnetic field with the coordinates of the proton being output in one centimeter intervals over the flight path. From these coordinates the line integral of the transverse component of the magnetic field was computed over the angular range of the monitor. The angular dependence of the integral was found to be a linear function of the angle in the region of the monitor. As shown in Figure 6.2 the integral could be parameterized by

$$\int \underline{B} \times d\underline{\ell} = 3.71(\theta) - 15.15 \quad (6.2)$$

where the angle θ is measured in degrees with respect to the direction of \underline{B} . At a fixed angle the variation of the line integral over the range of momenta relative to this experiment was less than 1%. Having determined the values of the line integral the magnetic deflections were calculated using the expression found in Section 3.4.

FIGURE 6.2
LINE INTEGRAL OF THE B FIELD



6.2 Background Subtractions

The opening angle and the coplanar angle, defined as the angle between the recoil nucleon momentum and the normal to the scattering plane where the scattering plane is that plane which contains the momentum vector of both incident and scattered particle, were constructed for each event that triggered the monitor. Momentum conservation requires that for proton proton elastic scattering with the target particle at rest the recoil nucleon's momentum must lie in the scattering plane. Thus the coplanar angle must be 90° . This restriction does not apply to a proton scattering from a proton in a carbon nucleus whose constituent nucleons possess fermi motion. For the carbon events the fermi momentum of the nucleons was consistent with a gaussian distribution centered at approximately 170 meV/C in each of the three momentum coordinates. As a result the probability of the struck nucleon having zero component of fermi momentum in the normal direction was small.

Histograms of the coplanar and opening angle were made for each run in beam spin "up", "down" and "off" configurations. The coplanar and opening angle histograms contained essentially the same information, however the coplanar histograms were found to be more sensitive to geometry and thus provided better resolution.

For that reason coplanarity histograms were used for all calculations.

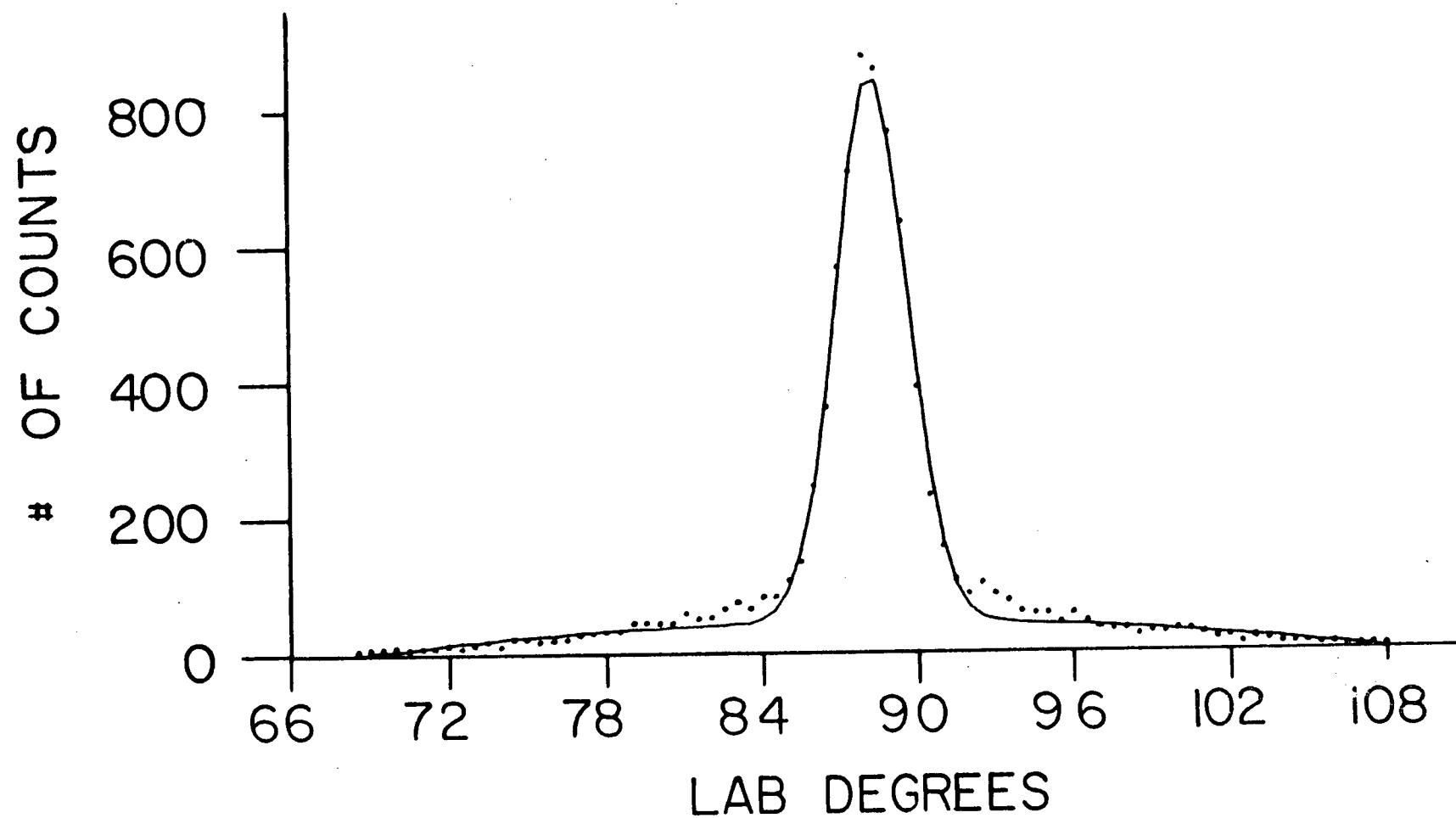
A sample coplanar histogram is shown in Figure 6.3. The parameterization is a gaussian elastic peak and a quadratic background. The five parameter fit used was

$$N = P1 + P3(\theta - P2)^2 + P4 \text{ EXP}(-.5((\theta - P2)/P5)^2) \quad (6.3)$$

where N is the number of counts. Though the scale in Figure 6.3 is in degrees the data were actually binned in half degree steps.

Two consistent features of these distributions were the points above the gaussian fit at approximately $\pm 6^\circ$ from the centre and the points above the peak near the centre. These features were present in all spin configurations. The points lying off the gaussian tails were in fact an indicator of good resolution in the chambers. These events have been assumed to be hydrogen signal that has been broadened by multiple scattering and energy losses. The chamber resolution was adequate to distinguish these events from the background. The points lying above the peak were also assumed to be hydrogen signal since, as explained earlier, the fermi momentum in carbon would not favour events to be peaked in this region. In the final analysis the quadratic background was integrated analytically using the parameter

FIGURE 6.3
COPLANAR HISTOGRAM



values P_1, P_2 and P_3 as determined by the fitting procedure. The number of protons elastically scattered into the monitor was determined by numerically summing all the events lying above the fitted background. In this way the multiple scattering events and the events lying above the gaussian peak were included in the elastic hydrogen count.

The ratio of hydrogen to background signal in the monitor was tabulated for each run in the configurations of spins parallel and spins antiparallel. The run averaged values of these ratios at each energy are tabulated in Table 6.1. The hydrogen to background ratios reflect the fact that the hydrogen in the target is polarized but the background is not. The terms parallel and antiparallel are only nominal since neither the incident protons nor the target protons were polarized exactly along the longitudinal. The spin precession in the bending magnet was different from 90° and the target was rotated through 12° . The polarization of the incident protons in the longitudinal direction depended firstly on the value of the beam polarization before precession, and secondly on the amount of precession in the bending magnet which was energy dependent. Hence because of the variation in the longitudinal component of beam polarization the ratio of hydrogen to background signal varied from run to run and had a definite energy

Table 6.1

Run Averaged Hydrogen To Background Ratios

<u>Energy</u>	<u>Spins Parallel</u>	<u>Spins Anti Parallel</u>
516.5	2.373 ± .082	1.960 ± .114
497.1	2.472 ± .098	1.966 ± .130
455.8	2.487 ± .140	2.020 ± .108
419.5	2.594 ± .255	2.026 ± .064
325.4	3.003 ± .276	1.851 ± .154
202.7	4.942 ± .828	2.303 ± .258

Table 6.2

Precession Angle ψ in the Bending Magnet

<u>Energy</u>	<u>ψ (Degrees)</u>
519.9	97.52
500.1	96.24
459.4	93.47
423.3	91.06
329.6	84.79
208.2	76.68

dependence. The ratios were used to check the consistency of the data and the run averaged values are included here to demonstrate in a systematic way that the monitor was sensitive to the polarization of hydrogen in the target.

6.3 The Fitting Equation

Using the density matrix formalism described in Section 2.1 the number of protons elastically scattered into the monitor for beam polarization P_b and target polarization P_T is

$$I^{\pm\mp} = I_0 \left\{ 1 + [C_{LL} \sin(\psi) \cos(12^\circ) - C_{SS} \cos(\psi) \sin(12^\circ) - C_{SL} \cos(\psi + 12^\circ)] P_b^{\pm} P_T^{\mp} \right\} \quad (6.4)$$

This equation was fitted by a non linear chi-squared minimization procedure to determine the target polarization. $I^{\pm\mp}$ is the number of protons elastically scattered into the monitor for beam polarization P_b^{\pm} and target polarization P_T^{\mp} . The superscripts + and - indicate positive and negative spin projections along the longitudinal direction. I_0 is proportional to the unpolarized rate in the monitor as described in the following. C_{LL} , C_{SS} and C_{SL} are the spin correlation parameters whose relation to the amplitudes of the scattering matrix is described by Hoshizaki.⁷ The subscripts S and L refer to the conventions of Figure 2.1. The contributions of the C_{SL} and C_{SS} components arise

from the 12° rotation of the target and the precession ψ in the bending magnet 4B3. Values of ψ calculated for a 35° bend at the precise beam energies are tabulated in Table 6.2.

The values of $I^{\pm\bar{4}}$ input into eq. 6.4 were the elastic hydrogen count obtained from the coplanar reconstructions, after correction for the detection efficiency of the monitor by the method outlined in Chapter IV. The correction for monitor efficiency was calculated on a run to run basis and applied to the hydrogen count. The monitor efficiency ranged from 95° to 99° throughout the experiment.

The unpolarized count I_0 is the number that would have been elastically scattered into the monitor for an unpolarized beam and unpolarized target. I_0 depends on the geometry of the monitor and on the incident rate. It was written as

$$I_0 = (KK) (N\phi) \quad (6.5)$$

where KK is a constant and $N\phi$ is the number in the incident beam as defined by the three beam defining counters. The constant KK represents the differential crosssection for unpolarized scattering integrated over the solid angle acceptance of the monitor. It was left as a free parameter of the fit.

The spin parameter values at the precise experimental energies and angles were obtained from David Bugg's phase shift analysis that makes use of the most recent nucleon-nucleon data from Argonne and Geneva.¹² Accuarate values of the beam polarization were calculated from the beam line polarimeter using the method described in Section 3.1. Values of the polarization parameter at 26° were also obtained from Bugg's phase shift analysis and are given in Table 6.3. Typical values of the beam polarization were 62°.

To obtain the target polarization, equation 6.4 was fitted with all data available at each energy in the four spin configurations. To allow for a variation in target polarization from run to run, it was written as

$$P_T^{\pm} = C^{\pm} \times 10^{-5} \times \int \text{NMR enhanced signal} \quad (6.6)$$

where C is a constant. Although C^+ and C^- are the same quantity the target spin up data was fit separately from the target spin down data as a systematic check and later recombined. Written in this way the constant taken together with the scaling factor is just

$$C \times 10^5 = \frac{P_{\text{thermal}}}{\int \text{NMR thermal signal}} \quad (6.7)$$

C was a free parameter of the fit and therefore was determined from the scattering data. This measurement of

Table 6.3

Values of the Polarization Parameter at 26° Lab

<u>Energy</u>	<u>P(26°)</u>
520.3	0.3992 ± .0077
501.0	0.3970 ± .0067
459.8	0.3670 ± .0064
423.7	0.3535 ± .0064
330.1	0.3314 ± .0036
209.0	0.2670 ± .0078

target polarization thus was completely independent of P_{thermal} and the NMR thermal signal. These were the two quantities that contributed the greatest uncertainty to the NMR measurement. The nuclear scattering measurement required only that the NMR enhanced signal be proportional to the nuclear polarization. It was free of the normalization uncertainties associated with the NMR method of measurement.

Hence the nuclear scattering data was used to determine the constant C which is the constant of proportionality relating the target polarization to the NMR signal when the target polarization is enhanced by the microwave radiation.

6.4 Error Analysis

The monitor accepted events scattered into a finite angular range. The spin correlation parameters are sensitive to angle. The forward arm of the monitor subtended an angular range of 19.7° at the target. The spin parameters are not linear over this angular range. For that reason cuts were made in the off line analysis to limit the angular acceptance to $\pm 3^\circ$ of a value chosen to optimize detection of the recoil particle in elastic two body events. This optimum angle varied slightly with energy due to relativistic effects.

For input into eq. 6.4, the average value of the scattering angle for all events accepted was determined at

each energy. This was done by inserting counters into the computing routine to average separately the scattering and recoil angle. In the centre of mass reference frame the opening angle must be 180° . Hence measurement of the recoil angle gives a second measure of the scattering angle. The two values thus obtained were averaged to form the quantity $\bar{\theta}$. The dispersion of the two values about $\bar{\theta}$ is their difference over $\sqrt{2}$ and the uncertainty in $\bar{\theta}$ is one-half of the difference in the measured values.

The composite quantity A, defined by

$$A = C_{LL} \sin(\psi) \cos(12^\circ) - C_{SS} \cos(\psi) \sin(12^\circ) - C_{SL} \cos(\psi + 12^\circ)$$

appearing in eq. 6.4 was evaluated at the angle $\bar{\theta}$ for each experimental energy and treated as a constant in the fitting program. Denoted hereafter by A, this quantity and the uncertainty in it was computed by rerunning the phase shift program,¹² each time using a different set of the existing world data as input. To ensure that the error on A was not underestimated, the error was evaluated from the maximum change in A plus the statistical variations.

There was also a small contribution to the uncertainty in A due to the uncertainty in $\bar{\theta}$. This error, denoted $\delta A(\bar{\theta})$, is just the dispersion of A about $A(\bar{\theta})$ for the two measurements of θ and was added in quadrature with the errors from the phase shift analysis to obtain an overall uncertainty in A given by δA .

The fitting procedure determined a value of C^+ and C^- along with their statistical errors at each energy except 497 meV. At this energy only one run of data was available with target spin "up" and hence only C^- was determined. The weighted mean of C^+ and C^- was formed at each energy using the expression

$$\bar{C} \pm \delta\bar{C} = \frac{\sum (C_i / \delta C_i^2)}{\sum (1 / \delta C_i^2)} \pm \sqrt{\frac{1}{\sum (1 / \delta C_i^2)}} \quad (6.8)$$

The result was six values of \bar{C} with its error $\delta\bar{C}$, where $\delta\bar{C}$ includes statistical errors on C_{\pm}^{\pm} and the total error on A. Finally the weighted mean of these six values was calculated to obtain the overall normalization constant C and its error.

Chapter VII

RESULTS AND CONCLUSION

7.1 Results

The results of the nuclear scattering measurement are presented in this section. The final values of A , $\bar{\theta}$ and $\delta A(\bar{\theta})$ are given in Table 7.1. A is the quantity that was defined in Section 6.4 and obtained from phase-shift analysis. $\bar{\theta}$ is the average scattering angle for all events accepted in the monitor as described in 6.4 and $\delta A(\theta)$ is the variation in A due to the uncertainty in θ . This error is much smaller than the errors on A arising from the phase-shift analysis.

The values of C^+ and C^- obtained by fitting the elastic scattering data are tabulated in Table 7.2 with their statistical errors. Also tabulated are \bar{C} , $\delta\bar{C}(A)$ and $\delta\bar{C}$, where \bar{C} is the weighted mean of C^+ and C^- , $\delta\bar{C}(A)$ is the relative error in \bar{C} due to the uncertainty in A and $\delta\bar{C}$ is the total error on \bar{C} . The total error on \bar{C} was obtained by adding $\delta\bar{C}(A)$ and the statistical error on \bar{C} in quadrature.

Table 7.1
Final Values of A, $\bar{\theta}$ and $\delta A(\bar{\theta})$

<u>Energy</u>	<u>A</u>	<u>$\bar{\theta}$ (c.m.)</u>	<u>$\delta A(\bar{\theta})$</u>
516.5	$0.2857 \pm .0361$	$74.43 \pm .30$.0022
497.1	$0.2822 \pm .0366$	$72.42 \pm .41$.0110
455.8	$0.2636 \pm .0330$	$71.74 \pm .45$.1600
419.5	$0.3255 \pm .0343$	$71.92 \pm .58$.0100
325.6	$0.5303 \pm .0325$	$72.07 \pm .56$.0098
202.7	$0.85.0 \pm .0400$	$70.56 \pm .56$.0068

The final value of C was obtained by taking the weighted mean of the six determinations of \bar{C} and its error $\delta \bar{C}$ appearing in Table 7.2. The result is

$$C = 0.9920 \pm .0336$$

For comparison, the value of C calculated from the NMR measurement using equation 6.7 was 1.035 but with an uncertainty of the order of 6%.

Values of the NMR enhanced signal polarization integrals for each run are given in Table 7.3. The error quoted is the standard deviation of all measurements made during the run. As mentioned previously the polarization integral was written onto tape following each event. The small deviation indicates the stability of the target polarization and the stability of the NMR enhanced signal.

Table 7.2

Final Values of \bar{C}

<u>Energy</u>	<u>C^+</u>	<u>C^-</u>	<u>\bar{C}</u>	<u>$\delta\bar{C}(A)$</u>	<u>$\delta\bar{C}$</u>
516.5	0.9118 \pm .0579	0.7970 \pm .0645	0.8606 \pm .0431	0.1092	0.1174
497.1		0.9715 \pm .0306	0.9715 \pm .0306	0.1271	0.1308
455.8	1.0283 \pm .0624	1.0736 \pm .0845	1.0443 \pm .0502	0.1322	0.1414
419.5	1.1212 \pm .0580	1.0870 \pm .0497	1.1015 \pm .0377	0.1177	0.1236
325.4	0.8611 \pm .0319	1.0925 \pm .0267	0.9972 \pm .0205	0.0622	0.0655
202.7	0.9443 \pm .0236	1.0414 \pm .0243	0.9914 \pm .0169	0.0466	0.0496

Table 7.3

NMR Polarization Integrals and Absolute
Target Polarization

Run #	NMR Polarization Integral		Absolute Target Polarization	
<u>500 MeV Target Polarization Negative</u>				
1	64737.1	± 26.7	.6422	± .0217
2	64825.4	± 28.0	.6431	± .0218
3	64829.5	± 21.8	.6431	± .0218
4	64757.6	± 22.2	.6424	± .0218
5	64685.5	± 17.8	.6417	± .0218
6	64975.8	± 20.8	.6446	± .0218
7	65036.2	± 31.8	.6452	± .0219
8	65237.8	± 32.9	.6472	± .0219
9	65021.8	± 30.9	.6450	± .0219
10	64937.1	± 37.8	.6442	± .0218
11	65786.8	± 50.8	.6526	± .0221
12	65696.5	± 56.9	.6517	± .0220
13	65717.4	± 44.2	.6519	± .0221
14	65846.9	± 46.0	.6532	± .0221
15	65678.3	± 60.7	.6515	± .0221
16	65733.7	± 57.7	.6521	± .0221
17	65706.2	± 34.6	.6518	± .0221
18	65738.4	± 32.3	.6521	± .0221
19	65657.9	± 45.8	.6513	± .0221
20	65672.8	± 54.7	.6515	± .0221
21	65741.8	± 40.0	.6522	± .0221
22	65693.1	± 19.1	.6517	± .0221
<u>500 MeV Target Polarization Positive</u>				
23	63530.9	± 16.8	.6302	± .0214
<u>210 MeV Target Polarization Positive</u>				
24	64504.1	± 31.8	.6399	± .0217
25	64504.8	± 21.5	.6399	± .0217
26	64624.8	± 24.8	.6411	± .0217
<u>210 MeV Target Polarization Negative</u>				
27	64940.2	± 26.4	.6448	± .0218
28	65001.3	± 31.5	.6448	± .0218

Table 7.3 - Continued

330 MeV Target Polarization Negative

29	64849.2 ± 33.0	.6433 ± .0218
30	64881.2 ± 58.2	.6436 ± .0218
31	64804.9 ± 55.3	.6429 ± .0218
32	64873.1 ± 45.5	.6435 ± .0218
33	64796.3 ± 58.7	.6428 ± .0218
34	64873.7 ± 58.3	.6435 ± .0218
35	64772.6 ± 33.9	.6425 ± .0218
36	64821.4 ± 57.3	.6430 ± .0218
37	64665.3 ± 39.7	.6415 ± .0217

330 MeV Target Polarization Positive

38	62233.7 ± 46.0	.6174 ± .0209
39	63702.5 ± 46.6	.6321 ± .0214
40	63830.1 ± 46.1	.6332 ± .0215
41	63970.6 ± 31.6	.6346 ± .0215

520 MeV Target Polarization Positive

42	63583.6 ± 29.6	.6307 ± .0214
43	63457.4 ± 32.9	.6295 ± .0213
44	63401.8 ± 29.0	.6289 ± .0213
45	63365.8 ± 37.1	.6286 ± .0213

520 MeV Target Polarization Negative

46	59312.2 ± 36.8	.5885 ± .0199
47	60173.9 ± 24.0	.5969 ± .0202
48	60265.0 ± 32.2	.5978 ± .0203

460 MeV Target Polarization Negative

49	59942.4 ± 28.1	.5946 ± .0202
50	59781.9 ± 41.2	.5930 ± .0201
51	59587.2 ± 25.9	.5911 ± .0200

460 MeV Target Polarization Positive

52	60961.2 ± 76.2	.6047 ± .0205
53	62355.2 ± 27.4	.6186 ± .0210
54	62376.7 ± 37.9	.6188 ± .0210
55	61450.1 ± 30.5	.6096 ± .0206
56	61419.1 ± 37.5	.6093 ± .0206
57	61385.2 ± 25.1	.6089 ± .0206

Table 7.3 - Continued425 MeV Target Polarization Positive

58	61374.7 \pm 34.9	.6088 \pm .0206
59	61306.5 \pm 50.0	.6082 \pm .0206
60	61167.8 \pm 32.4	.6068 \pm .0206

425 MeV Target Polarization Negative

61	54965.0 \pm 57.1	.5452 \pm .0184
62	56643.1 \pm 38.4	.5619 \pm .0190
63	56928.2 \pm 33.5	.5647 \pm .0194

The final target polarizations calculated using the value of C determined from the nuclear scattering measurement are also tabulated in 7.3.

7.2 Conclusion

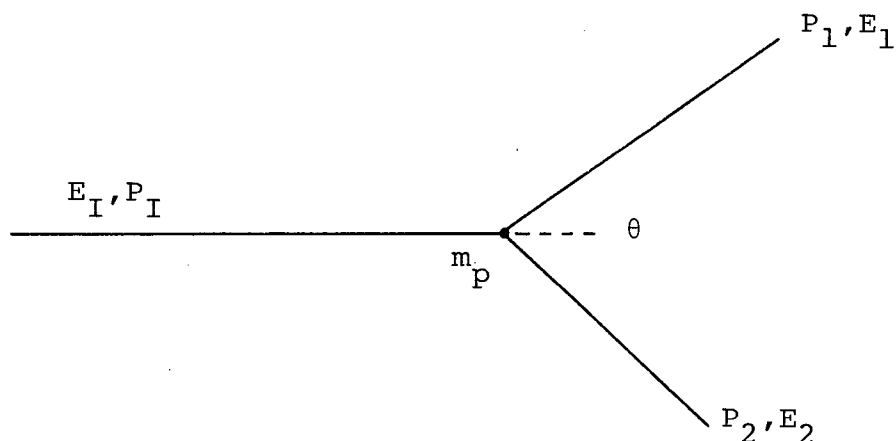
The absolute polarization of a dynamically polarized proton target has been measured to an accuracy of $\pm 2\%$ by observing the asymmetry in a proton beam scattered from the target. The analysis made use of existing information on the spin dependence of the nucleon nucleon interaction to account for the asymmetry that was observed. The measurement is in excellent agreement with an independent NMR determination of the target polarization, however the uncertainty has been substantially reduced. The largest contribution to the error in this measurement came from the phase shift analysis used to determine the asymmetry A . Improvement in the world nucleon nucleon data would lead to more accurate phase shift analyses and further reduce the uncertainty in this measurement.

REFERENCES

1. I.P. Auer et al., Phys. Lett. 67B, 113 (1977);
Phys. Rev. Lett. 41, 341 (1978).
2. E.K. Biegert et al., Phys. Rev. Lett. 44, 558 (1975).
3. E.F. Parker et al., Phys. Rev. Lett. 31, 783 (1973).
4. C.L. Hollas, Phys. Rev. Lett. 44, 1186 (1980).
5. B. Coyler, Rutherford Laboratory Report, RHEL/R 138 (1966).
6. L. Wolfenstein, Ann. Rev. Nuc. Sci. 6, 43 (1956).
7. N. Hoshizaki, Suppl. Progr. Theor. Phys. 42, 107 (1968).
8. C.D. Jeffries, "Dynamic Nuclear Orientation", John Wiley & Sons, Inc., 1963.
9. A. Abragam, "The Principles of Nuclear Magnetism", Oxford University Press, 1961.
10. C. Amsler et al., J. Phys. G. 4, 1047 (1978).
11. D. Gifford, "Proceedings of the Second Workshop on Polarized Targets", eds. G. Court, S. Cox, D. Cragg and T. Niinikoski, Rutherford High Energy Lab Publication, RL-80-080, October 1980.
12. D.V. Bugg, Private Communication.

APPENDIX A

Derivation of Equation 6.1



$$P_2^2 = P_1^2 + P_I^2 - 2P_1P_I \cos(\theta)$$

$$E_I + m_p + E_1 + E_2$$

Therefore

$$E_2^2 = E_I^2 + m_p^2 + 2E_I m_p - 2E_I E_1 - 2m_p E_1$$

but

$$E_2^2 = P_2^2 + m_p^2, \quad E_I^2 = P_I^2 + m_p^2$$

$$P_2^2 + m_p^2 = P_I^2 + m_p^2 + m_p^2 + P_1^2 + m_p^2 + 2E_I m_p - 2E_I E_1 - 2m_p E_1$$

$$P_2^2 - P_I^2 - P_1^2 = 2m_p^2 + 2E_I m_p - 2E_I E_1 - 2m_p E_1$$

$$\text{replace } P_2^2 = P_1^2 + P_I^2 - 2P_1P_I \cos(\theta)$$

$$-P_I^2 - P_1^2 + P_1^2 + P_I^2 - 2P_1P_I \cos(\theta) = 2m_p^2 + 2E_I m_p - 2E_I E_1 - 2m_p E_1$$

$$-P_1P_I \cos\theta = m_p^2 + E_I m_p - E_I E_1 - m_p E_1$$

$$E_1 (E_I + m_p) = m_p^2 + E_I m_p + P_1P_I \cos(\theta)$$

$$E_1 = \frac{m_p^2 + E_I m_p + p_1 P_I \cos(\theta)}{(E_I + m_p)}$$

now square both sides and substitute for E_1^2

$$\begin{aligned} p_1^2 + m_p^2 &= \\ \frac{m_p^4 + E_I^2 m_p^2 + p_1^2 P_I^2 \cos^2(\theta) + 2m_p^3 E_I + 2m_p^2 p_1 P_I \cos(\theta) + 2E_I m_p p_1 P_I \cos(\theta)}{(E_I + m_p)^2} \end{aligned}$$

$$(p_1^2 + m_p^2)(E_I^2 + m_p^2 + 2E_I m_p) =$$

$$m_p^4 + E_I^2 m_p^2 + p_1^2 P_I^2 \cos^2(\theta) + 2m_p^3 E_I + 2m_p^2 p_1 P_I \cos(\theta) + 2E_I m_p p_1 P_I \cos(\theta)$$

multiplying out the L.H.S. and cancelling terms gives

$$p_1^2 (E_I^2 + m_p^2 + 2E_I m_p - p_1^2 \cos^2(\theta)) + (-2p_1 m_p^2 \cos(\theta) - 2E_I m_p p_1 \cos(\theta)) = 0 .$$